

1 **Light-absorbing black carbon and brown carbon components of smoke aerosol from**
2 **DSCOVR EPIC measurements over North America and Central Africa**

3
4 Myungje Choi^{1,2}, Alexei Lyapustin², Gregory L. Schuster³, Sujung Go^{1,2}, Yujie Wang^{1,2}, Sergey
5 Korkin^{1,2}, Ralph Kahn^{2,4}, Jeffrey S. Reid⁵, Edward J. Hyer⁵, Thomas F. Eck^{1,2}, Mian Chin², David
6 J. Diner⁶, Olga Kalashnikova⁶, Oleg Dubovik⁷, Jhoon Kim⁸, Hans Moosmüller⁹

7
8 ¹Goddard Earth Sciences Technology and Research (GESTAR) II, University of Maryland
9 Baltimore County, Baltimore, MD, USA

10 ²NASA Goddard Space Flight Center, Greenbelt, MD, USA

11 ³NASA Langley Research Center, Hampton, VA, USA

12 ⁴Laboratory for Atmospheric and Space Physics, The University of Colorado Boulder, Boulder,
13 CO, USA

14 ⁵US Naval Research Laboratory, Monterey, CA, USA

15 ⁶Jet Propulsion Laboratory, California Institute of Technology, Pasadena, CA, USA

16 ⁷Laboratoire d'Optique Atmosphérique, Université de Lille-1, CNRS, Villeneuve d'Ascq, France

17 ⁸Department of Atmospheric Sciences, Yonsei University, Seoul, Republic of Korea

18 ⁹Laboratory for Aerosol Science, Spectroscopy, and Optics, Desert Research Institute, Reno, NV,
19 USA

20

21 Correspondence to: Myungje Choi (myungje.choi@nasa.gov)

22

23 **Abstract**

24 Wildfires and agricultural burning generate seemingly increasing smoke aerosol emissions,
25 impacting societal and natural ecosystems. To understand smoke's effects on climate and public
26 health, we analyzed the spatiotemporal distribution of smoke aerosols, focusing on two major
27 light-absorbing components, black carbon (BC) and brown carbon (BrC) aerosols. Using NASA's
28 Earth Polychromatic Imaging Camera (EPIC) instrument aboard the NOAA's Deep Space Climate
29 Observatory (DSCOVR) spacecraft, we inferred BC and BrC volume fractions and particle mass
30 concentrations based on spectral absorption provided by the Multi-Angle Implementation of
31 Atmospheric Correction (MAIAC) algorithm with 1-2 hours temporal resolution and ~10 km
32 spatial resolution over North America and Central Africa. Our analyses of regional smoke
33 properties reveal distinct characteristics for aerosol optical depth (AOD) at 443 nm, spectral single
34 scattering albedo (SSA), aerosol layer height (ALH), and BC and BrC amounts. Smoke cases in
35 North America show extremely high AOD up to 6, with elevated ALH (6-7 km) and significant
36 BrC components up to 250 mg/m² along the transport paths, whereas the smoke aerosols in Central
37 Africa exhibited stronger light absorption (i.e., lower SSA) and lower AOD, resulting in higher
38 BC mass concentrations and similar BrC mass concentrations than the cases in North America.
39 Seasonal burning source locations in Central Africa following the seasonal shift of Inter Tropical
40 Convergence Zone and diurnal variations in smoke amounts were also captured. Comparison of
41 retrieved AOD₄₄₃, SSA₄₄₃, SSA₆₈₀, and ALH with collocated AERONET and CALIOP
42 measurements shows agreement with *rmse* of 0.2, 0.03-0.04, 0.02-0.04, and 0.8-1.3 km,
43 respectively. Analysis of spatiotemporally average reveals distinct geographical characteristics in
44 smoke properties closely linked to burning types and meteorological conditions. Forest wildfires
45 over western North America generated smoke with small BC volume fraction of 0.011 and high
46 ALH with large variability (2.2 ± 1.2 km), whereas smoke from wildfires and agricultural burning
47 over Mexico region shows more absorption and low ALH. Smoke from savanna fires over Central
48 Africa has the most absorption with high BC volume fraction (0.015) and low ALH with small
49 variation (1.8 ± 0.6 km) among the analyzed regions. Tropical forest smoke was less absorbing
50 and had a high variance in ALH. We also quantify the estimation uncertainties related to the
51 assumptions of BC and BrC refractive indices. The MAIAC EPIC smoke properties with BC and
52 BrC volume and mass fractions and assessment of layer height provide observational constraints
53 for radiative forcing modeling and air quality and health studies.

54
55 **Keywords:** EPIC, light absorbing smoke aerosol component, BC, BrC

56

57 **1. Introduction**

58 Natural and anthropogenic fires affect and shape nearly every terrestrial vegetated
59 ecosystem on the planet (Pausas and Keeley, 2009; Bond and Keeley, 2005), and their emissions
60 have long been known to affect the global atmospheric composition and radiative budget (Hobbs
61 et al., 1997; Seiler and Crutzen, 1980). Recent climate changes and anthropogenic activities have
62 affected wildfire and agricultural fire occurrence in many regions (Liu et al., 2010; Dennison et
63 al., 2014). Global monitoring of atmospheric smoke aerosol chemical, optical, and microphysical
64 properties is important to quantify the impacts of increasing biomass burning on climate and air
65 quality. However, the current understanding of smoke aerosol radiative forcing is still insufficient
66 due to its high spatiotemporal variability in combination with the dynamic nature of smoke and
67 variability of its physical and optical properties (IPCC, 2023).

68 One characteristic that distinguishes smoke particle components from other components is
69 light absorption. Absorbing particle components converting incident electromagnetic energy into
70 thermal energy results in heating of both the particles and the ambient surrounding atmosphere.
71 Aerosol light absorption greatly affects direct radiative forcing and atmospheric stability and
72 convections (IPCC, 2023; Bellouin et al., 2005; Yu et al., 2002). Smoke particles emitted from
73 biomass burning typically contain two major light-absorbing carbonaceous components: black
74 carbon (BC) and brown carbon (BrC). The proportions of these light-absorbing components and
75 their mixing ratios determine the spectral absorption characteristics (e.g., Jacobson, 2001;
76 Chakrabarty et al., 2023).

77 BC is a byproduct of the incomplete combustion of carbonaceous materials. There is no
78 specific chemical makeup of BC and depending on measurement techniques it is also called soot,
79 elemental carbon, or light-absorbing carbon (Reid et al., 2005a; Moosmüller et al., 2009; Andreae
80 and Gelencsér, 2006). BC is visibly black, resulting in a high and spectrally invariant imaginary
81 refractive index (~ 0.79) across UV-visible wavelengths (Bond and Bergstrom, 2006). During
82 combustion, tiny BC spherules are aggregated with each other and grow by absorbing surrounding
83 gas-phase molecules into large particles with a complex, generally fractal-like morphology
84 (Moosmüller et al., 2009). Emitted atmospheric BC particles are generally hydrophobic (Petters et
85 al., 2009), but can quickly evolve to hydrophilic if they acquire water-soluble coatings upon
86 emission or during atmospheric aging (Tritscher et al., 2011). Atmospheric aging processes change
87 BC's physical and chemical particle structure (Corbin et al., 2023; Bhandari et al., 2019; Sengupta
88 et al., 2020), as well as optical properties (Gyawali et al., 2017; Kleinman et al., 2020; Reid et al.,
89 2005b). Particle evolutions combine with the high spatial and temporal variability of the sources
90 to make the net radiative effects of these particles highly uncertain (Bond et al., 2013; IPCC, 2023;
91 Chakrabarty et al., 2023).

92 The largest carbonaceous aerosol component directly emitted from biomass burning is
93 organic carbon (OC; e.g., Andreae and Merlet, 2001; Andreae, 2019 and references therein). This
94 study defines the OC with significant light absorbing property in the tropospheric solar spectrum
95 as brown carbon (BrC; e.g., Laskin et al., 2015). BrC exhibits spectral variability, absorbing more
96 ultraviolet (UV) and short visible light than long visible light, resulting in a reddish or brownish

97 appearance. Its imaginary refractive index varies spectrally, with generally higher values at shorter
98 (i.e., UV) wavelengths and decreasing toward longer, visible and infrared (IR) wavelengths
99 (Kirchstetter et al., 2004). BrC emission and the chemical processes responsible for BrC formation
100 are complex and not yet fully understood. Some studies suggest BrC consists primarily of water-
101 soluble organic carbon compounds and humic-like substances (Sun et al., 2007; Phillips and Smith,
102 2014; Hoffer et al., 2006) whereas others suggest that non-polar compounds can absorb more light
103 than polar compounds, especially in the UV and short-wavelength visible (Sengupta et al., 2018).
104 BrC compounds can be released from smoldering biomass burning or formed through secondary
105 organic aerosol processes in the atmosphere (Chakrabarty et al., 2010; Laskin et al., 2015). BC
106 coated with non-absorbing organic and inorganic may exhibit a similar wavelength dependence of
107 absorption, with higher values at shorter wavelengths (Wang et al., 2016). This similarity makes
108 it challenging to differentiate between BrC and coated BC based on spectral absorption alone.
109 Therefore, our "BrC" results may include contributions from coated BC.

110 According to the latest Intergovernmental Panel on Climate Change (IPCC) report (IPCC,
111 2023), the present day global effective radiative forcing of black carbon from fossil fuel and biofuel
112 is estimated at 0.107 W m^{-2} with a 5-95% uncertainty range of -0.202 to 0.417 W m^{-2} , with
113 respect to the pre-industrial time of 1750. In contrast, primary organic aerosols from fossil fuel
114 and biofuel, related to OC, exhibit a cooling effect of -0.209 W m^{-2} , with an uncertainty range of
115 -0.439 to -0.021 W m^{-2} . Although BrC is not directly considered in this assessment, its radiative
116 forcing is partially accounted for within primary organic aerosol, biomass burning, or secondary
117 organic aerosols in some global aerosol models. Combining ground-based measurements and
118 chemical transport modeling, Jo et al. (2016) attributed non-BC absorption to BrC and estimated
119 BrC fraction as 21% of the global mean surface OC concentration, significantly impacting ozone
120 photochemistry by altering the UV radiation field. Zhang et al. (2020) estimated that the global
121 BrC direct radiative effect is 0.10 W m^{-2} , suggesting that BrC can heat the tropical mid and upper
122 troposphere more than BC. Still, much uncertainty remains about BrC due to limited measurements
123 and the complex processes involved, challenging accurate estimates of its radiative impact on
124 climate (Liu et al., 2020).

125 Intensive *in situ* measurements have been instrumental in identifying the composition-
126 related spectral light-absorption properties of smoke plumes, as summarized in Bond and
127 Bergstrom (2006), Andreae and Gelencsér (2006), Moosmüller et al. (2009), and Samset et al.
128 (2018). These measurements have enabled remote sensing techniques to differentiate between
129 various light-absorbing components in smoke plumes. For example, the Aerosol Robotic Network
130 (AERONET) sunphotometers routinely provide aerosol optical and microphysical properties,
131 including spectral refractive indices from many sites worldwide (Holben et al., 1998; Dubovik and
132 King, 2000). Using AERONET inversion data, Schuster et al. (2016) inferred aerosol components
133 over smoke- and dust-dominated regions by matching AERONET spectral refractive index to
134 mixtures of components with different assumed optical properties. Specific absorbing components
135 were assumed as inclusions: BC and BrC for smoke and iron oxides of hematite and goethite for
136 dust aerosols. Wang et al. (2013) and Choi et al. (2020) applied a similar approach to East Asia

137 sites. The synergy between visible/near-IR AERONET measurement and UV/visible multifilter
138 rotating shadowband radiometer (MFRSR) measurements confirmed the sensitivity of spectral
139 absorption consistent with a BrC component (Mok et al., 2016, 2018).

140 Inferring aerosol composition from satellites is more challenging than from ground-based
141 remote sensing due to the need to account for the surface contribution to the top-of-atmosphere
142 signal, and the much greater range of conditions that space-borne instrument samples. Retrieving
143 aerosol absorptions using multi-spectral bands in near UV wavelengths has been applied to
144 instruments such as the Total Ozone Mapping Spectrometer (TOMS) and the Ozone Monitoring
145 Instrument (OMI), which have data records spanning decades, as well as more recently launched
146 instruments like the TROPOspheric Monitoring Instrument (TROPOMI) and Earth Polychromatic
147 Imaging Camera (EPIC; Torres et al., 1998, 2007, 2013, 2020; Ahn et al., 2021). The fraction of
148 retrieved single scattering albedo (SSA) within the expected error, defined as a fraction within
149 ± 0.03 from AERONET SSA, is approximately 50%, based on long-term and global validation
150 across these sensors (Ahn et al., 2021; Torres et al., 2020).

151 The Generalized Retrieval of Aerosol and Surface Properties (GRASP) algorithm
152 (Dubovik et al., 2011, 2014) utilizes the multi-angle, multi-channel, and both radiometric and
153 polarimetric measurements from the POLarization and Directionality of the Earth's Reflectances
154 (POLDER) instruments. With increased information incorporated by a multi-pixel multi-temporal
155 smoothness constraint, the GRASP algorithm retrieves aerosol optical depth (AOD), particle size
156 information, and absorption, showing robust agreement with global AERONET measurements
157 (Chen et al., 2020). Recent improvement of the GRASP algorithm included the direct estimation
158 of aerosol chemical composition concentrations without the need for intermediate steps such as
159 retrieving refractive indices and particle size distributions (Li et al., 2019, 2020). The Multi-angle
160 Imaging SpectroRadiometer (MISR) research algorithm also accounts for black-smoke and brown-
161 smoke aerosol models (Limbacher et al., 2022), analogous to the BC and BrC components in this
162 study, and is utilized to analyze fractional AODs along transport paths (Junghenn Noyes et al.,
163 2020a, b, 2022). Still, it is worth noting that POLDER and MISR measurements are limited to
164 visible and near-infrared (NIR) channels and do not include ultraviolet (UV) channels, where
165 spectral absorption due to BC and in particular BrC is more pronounced.

166 The EPIC sensor aboard the Deep Space Climate Observatory (DSCOVR) spacecraft has
167 provided UV-near IR measurements of Earth since 2015 (Marshak et al., 2018). Recent studies by
168 (Lyapustin et al., 2021b) have utilized the Multi-Angle Implementation of Atmospheric Correction
169 (MAIAC) processing of EPIC measurements to derive AOD and spectral absorption. It enables
170 inferring aerosol chemical compositional differences, such as BC and BrC in smoke aerosol
171 plumes and iron oxides (e.g., hematite and goethite) in dust aerosol plumes. DSCOVR's orbit
172 around the Lagrange-1 point, where the spacecraft remains stably positioned between the sun and
173 Earth, allows for global monitoring multiple times per day during the daylight time with a temporal
174 resolution of 1-2 hours. In our study, we used EPIC measurements to infer BC and BrC volume
175 fractions and mass concentrations in smoke plumes and identified distinct smoke properties over

176 North America and Central Africa. The estimation of iron oxides in dust aerosols using the EPIC
177 MAIAC EPIC product was addressed in Go et al. (2022).

178 The structure of the paper is as follows. Section 2 introduces the EPIC-MAIAC EPIC
179 smoke aerosol retrieval algorithm and describes the methodology for inferring BC and BrC volume
180 fractions and mass concentrations. It also includes descriptions of study regions and of AERONET
181 and CALIOP validation datasets. In Section 3, we analyzed individual smoke cases over North
182 America and Central Africa, and provided validation of AOD, spectral SSA, and aerosol layer
183 height (ALH). Additionally, time-integrated regional properties, including BrC/BC ratios, and
184 uncertainty estimates based on different inclusion assumptions are discussed. Finally, Section 4
185 offers summary and concluding remarks.

186 2. Data and methods

187 2.1 MAIAC EPIC processing algorithm

188 EPIC measurements cover the entire sunlit hemisphere of Earth with ten narrowband
189 spectral channels from 317.5 to 779.5 nm. The spatial resolution of EPIC is ~8-16 km at nadir,
190 degrading toward the edge of the image. MAIAC EPIC algorithm grids and processes L1B data at
191 10 km resolution providing an oversampling. DSCOVR's Lagrange point 1 orbit between the Earth
192 and the Sun (~1.5 million kilometers) enables global multi-temporal daytime measurements, with
193 10–12 observations in boreal summer and 6-7 observations in winter at mid-latitudes and little
194 seasonal change in tropical latitudes. Detailed information on EPIC measurements can be found
195 in Marshak et al. (2018). Following the MAIAC Moderate Resolution Imaging Spectroradiometer
196 (MODIS) algorithm (Lyapustin et al., 2018), the standard MAIAC processing offers cloud
197 detection, atmospheric correction, and AOD with regionally specified background aerosol models
198 ("background AOD"; Lyapustin et al., 2021a). In addition, a newly developed absorbing smoke or
199 dust aerosol retrieval process was applied to both land and ocean pixels. Smoke/dust detection and
200 separation are based on various tests including UV aerosol index and spectral AOD shape. As
201 EPIC band configuration does not allow to distinguish between smoke and dust aerosols, the dust
202 retrievals are only performed over pre-defined dust regions whereas smoke retrievals are
203 performed elsewhere globally (Lyapustin et al., 2021b).

204 The full algorithm description ~~is will be~~ given elsewhere ~~(Lyapustin et al., in preparation)~~;
205 here we provide a very brief overview to facilitate understanding of our results. The novel version
206 3 (v3) MAIAC algorithm represents spectral aerosol absorption with two parameters, the
207 imaginary refractive index at 680 nm (k_0) and spectral absorption exponent (SAE), using a
208 conventional power-law expression, $k_\lambda = k_0(\lambda/\lambda_0)^{-SAE}$ where $\lambda_0 = 680$ nm. The real refractive
209 index is assumed to have a spectrally invariant value of 1.51 (Lyapustin et al., 2021b). The particle

210 log-normal volume size distribution is defined as $\frac{dV(r)}{d\ln(r)} = \sum_{i=1}^2 \frac{C_{vi}}{\sqrt{2\pi}\sigma_i} e^{-\frac{1}{2}\left(\frac{\ln(r)-\ln(r_{v,i})}{\sigma_i}\right)^2}$, where i

211 indicates each mode (fine and coarse), r is the particle radius, $r_{v,i}$ is the volume mean radius, σ_i is

212 the geometric standard deviation, $c_{v,i}$ is the volumetric concentration. For smoke aerosols, we
213 assumed fine mode volume mean radius (0.14 μm) and geometric standard deviation (0.4 μm),
214 coarse mode volumetric mean radius (2.8 μm) and geometric standard deviation (0.6 μm). In
215 MAIAC v3, the Levenberg-Marquardt nonlinear optimal fitting algorithm (Levenberg, 1944;
216 Marquardt, 1963) is used to simultaneously retrieve four parameters $\{AOD_{443}, k_0, SAE, ALH\}$ by
217 matching EPIC measurements at UV to NIR wavelengths, including oxygen A and B bands. The
218 algorithm uses pre-computed look-up tables (LUTs) covering the full range of expected variability
219 of the above parameters. The maximum value of AOD at 443 nm in the algorithm is set to 6.
220 Vertically, the aerosol is modeled by a single 2 km-thick aerosol layer placed at different altitudes
221 in the atmosphere, and the reported ALH is defined as the midpoint height of the layer. To avoid
222 systemic biases in absorption, this retrieval is performed over detected absorbing smoke/dust
223 pixels when the retrieved AOD, based on the background aerosol model with fixed regional
224 properties, is greater than 0.4. Note that although smoke retrievals are limited with “background
225 $AOD_{443} > 0.4$ ” the retrieved smoke AOD_{443} could be lower than 0.4 due to different assumption
226 of microphysical properties and simultaneous retrieval of spectral absorption and ALH.

227 2.2 MAIAC smoke composition inference

228 Given a very different spectral absorption of BC (high and spectrally fairly flat) and BrC
229 (low and strongly increasing towards UV), the retrieved spectral absorption can be used to derive
230 fractions of absorbing components. We assume that smoke aerosols consist of a non-absorbing
231 host and two absorbing species, BC and BrC, with internal mixing based on Maxwell Garnett
232 effective medium approximation (MG-EMA) (Bohren and Huffman, 1998; Schuster et al., 2005,
233 2016). The MG-EMA is suitable for characterizing smoke particles and is computationally
234 efficient (Garnett, 1904; Bohren and Huffman, 1998; Schuster et al., 2005; Markel, 2016a, b). For
235 that reason, it is widely used for inferring aerosol compositions from ground-based or satellite-
236 based remote sensing (Li et al., 2019; Schuster et al., 2005, 2016; Choi et al., 2020; Go et al., 2022).
237 Studies showed that different internal mixing rules, such as Bruggeman approximation or volume
238 averaging, yields similar results to the MG-EMA for inferring smoke components (Schuster et al.,
239 2016; Li et al., 2019; and references therein). External mixing could be assumed, resulting in lower
240 absorption than internal mixing (Lesins et al., 2002; Lack et al., 2012), but most BC particles exist
241 internally mixed with other components in biomass burning plumes (Schwarz et al., 2008). The
242 non-absorbing host (or medium) represents a mixture of non-absorbing or low-absorbing
243 components in smoke, such as non-absorbing OC, sulfate, nitrate, and/or ammonium. Although
244 there are various ranges of refractive indices for both BC and BrC based on literature and
245 experiments, this study assumes fixed refractive index to estimate their fractions from the limited
246 information of the retrieved optical properties. The BC refractive index assumes Bond and
247 Bergstrom (2006)’s suggestion of spectrally flat with a real part (n) of 1.95 and an imaginary part
248 (k) of 0.79 for the visible spectrum (i.e., 400 – 700 nm). Spectral dependence of k for BrC is based
249 on Kirchstetter et al. (2004), whereas a constant real part of 1.54 was assumed based on Li et al.
250 (2019). For a spectrally flat and non-absorbing host we assume $n=1.51$, consistent with the smoke

251 aerosol model in the MAIAC EPIC algorithm, and $k=10^{-9}$ based on Kalashnikova et al. (2018).
 252 Table 1 summarizes the spectral refractive indices of BC, BrC and host. Please note that a
 253 sensitivity test for different assumptions regarding BC and BrC imaginary refractive indices
 254 affecting their volume fractions is detailed in Sec 3.5.

255
 256 Table 1. Spectral refractive indices of smoke aerosol components at EPIC wavelengths.

Wavelengths (nm)	BC		BrC		host	
	n	k	n	k	n	k
340	1.95	0.790	1.54	0.187	1.51	10^{-9}
388	1.95	0.790	1.54	0.125	1.51	10^{-9}
443	1.95	0.790	1.54	0.070	1.51	10^{-9}
680	1.95	0.790	1.54	0.003	1.51	10^{-9}

257
 258 The MG-EMA equation for smoke aerosol mixtures, as described in Bohren and Huffman
 259 (1998) and Schuster et al., (2005), is presented below.

$$260 \quad \epsilon_m = \epsilon_h \left[1 + \frac{3 \left(f_{BC} \frac{\epsilon_{BC} - \epsilon_h}{\epsilon_{BC} + 2\epsilon_h} + f_{BrC} \frac{\epsilon_{BrC} - \epsilon_h}{\epsilon_{BrC} + 2\epsilon_h} \right)}{1 - f_{BC} \frac{\epsilon_{BC} - \epsilon_h}{\epsilon_{BC} + 2\epsilon_h} - f_{BrC} \frac{\epsilon_{BrC} - \epsilon_h}{\epsilon_{BrC} + 2\epsilon_h}} \right]$$

261 Here, ϵ_m , ϵ_h , ϵ_{BC} , and ϵ_{BrC} represent the complex dielectric functions of the mixture, host,
 262 BC, and BrC, respectively, and f_{BC} and f_{BrC} denote the volume fractions of BC and BrC,
 263 respectively. Note that identical BC and BrC components are assumed for both fine and coarse
 264 modes. Throughout plume evolution, different processes such as oxidation, hydration, deposition
 265 of volatile organics onto existing particles, or new particle formation, may lead to larger particle
 266 sizes. Consequently, the fine-mode and coarse-mode components in smoke aerosols could exhibit
 267 differences. Schuster et al. (2016) also accounted for different component combinations between
 268 fine and coarse modes, considering dust particles for the coarse mode. It should be noted that
 269 biomass burning aerosols are strongly dominated by the fine mode component, with typically only
 270 a minor coarse mode AOD. However, the MAIAC EPIC processing relies on a static particle size
 271 distribution, and dynamic separation of fine and coarse modes is challenging with limited
 272 measurement information.

273 The refractive indices of the mixture can be determined using the following equations:

$$274 \quad n = \sqrt{\frac{\sqrt{\epsilon_r^2 + \epsilon_i^2} + \epsilon_r}{2}},$$

$$275 \quad k = \sqrt{\frac{\sqrt{\epsilon_r^2 + \epsilon_i^2} - \epsilon_r}{2}},$$

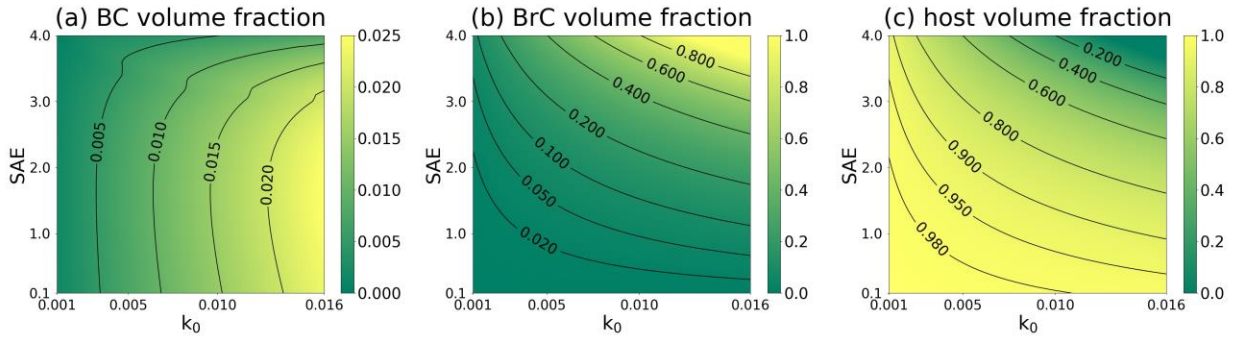
276 where ϵ_r and ϵ_i represent the real and imaginary parts of the mixture dielectric function ϵ_m . Given
 277 fixed spectral refractive indices of the host and inclusions (BC and BrC), the mixture refractive
 278 indices are determined by the volume fractions of two inclusions (f_{BC} and f_{BrC}).

279 Subsequently, we utilized the Levenberg-Marquardt nonlinear least-square fitting method
 280 (Levenberg, 1944; Marquardt, 1963; Press et al., 2007) to derive the volume fractions of inclusions
 281 by comparing inferred and calculated refractive indices with the MG-EMA. Retrieved k_0 and SAE
 282 were converted into spectral imaginary refractive indices (k_λ for λ of 340, 380, 443, and 680 nm)
 283 and matched with theoretical values of a mixture to find solutions for f_{BC} and f_{BrC} .

284 Fig. 1 illustrates the derivable BC, BrC, and host volume fractions for assumed ranges of
 285 k_0 (0.001–0.016) and SAE (0.1–4) in the MAIAC EPIC algorithm. Available f_{BC} , f_{BrC} , and f_{host}
 286 ranges are from 0 to 0.025, 0.994, and 0.998, respectively, where $f_{host} = 1 - f_{BC} - f_{BrC}$. The
 287 maximum f_{BC} of 0.025 can be found in the condition of maximum k_0 of 0.016. A high f_{BrC} near
 288 one can be retrieved when both k_0 and SAE are high. The host volume fraction (f_{host}) shows an
 289 opposite tendency to f_{BrC} and is low when both k_0 and SAE are high. Conversion from retrieved
 290 k_0 and SAE to volume fractions follows the presented distributions.

291 It should be mentioned that the upper limit of $k_0=0.016$ was found empirically based on
 292 limited EPIC regional processing, and then confirmed by the global processing of EPIC data.
 293 However, this limit may be increased in the future based on detailed analysis of EPIC retrievals,
 294 in particular because AERONET inversion retrievals often show higher values, for example in
 295 Central and southern Africa savanna burning region (Eck et al., 2003).

296



297
 298 Figure 1. The range of volume fractions for (a) BC, (b) BrC, and (c) host across different values
 299 of k_0 and SAE.

300

301 The inferred volume fractions of BC and BrC can be converted to column-integrated
 302 volume concentrations as,

303

$$C_V = C_{Vf} + C_{Vc} = \frac{AOD_f}{h_f} + \frac{AOD_c}{h_c},$$

304

$$AOD_f = AOD \cdot \left(\frac{C_{Vf}}{C_{Vf} + C_{Vc}} \right),$$

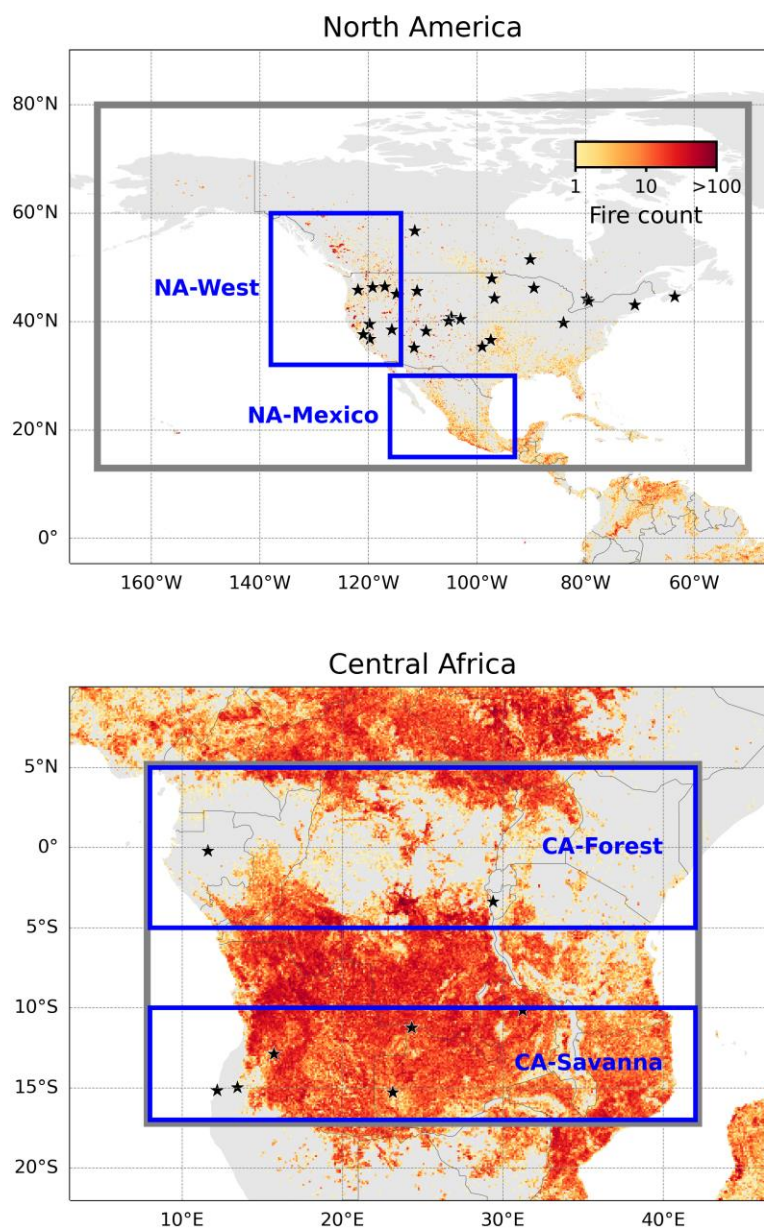
305

$$AOD_c = AOD \cdot \left(\frac{C_{Vc}}{C_{Vf} + C_{Vc}} \right),$$

306 where C_v is the column-integrated volume concentration with a unit of $\mu\text{m}^3/\mu\text{m}^2$, the subscripts f
307 and c indicate fine-mode and coarse-mode, respectively. Despite the regional dependence of $\frac{C_{vc}}{C_{vf}}$
308 in the 4D-retrieval algorithm for smoke, we assume a static $\frac{C_{vc}}{C_{vf}}$ of 0.7 for BC and BrC processing
309 to maintain consistency and reduce regional discrepancies arising from the ratio. Hygroscopicity
310 was neglected by using a static AOD per volume concentration regardless of relative humidity.
311 Given the size distribution and n , h_f of $8.43 \mu\text{m}^2/\mu\text{m}^3$ is fine mode AOD_{443} per unit volume
312 concentration ($\mu\text{m}^3/\mu\text{m}^2$) and h_c of $0.72 \mu\text{m}^2/\mu\text{m}^3$ is coarse mode AOD_{443} per unit volume
313 concentration, as calculated based on Mie theory in the MAIC EPIC smoke model (Lyapustin et
314 al., 2021b). Given the complex refractive indices, size distribution with fine-mode or coarse-mode
315 only, and non-sphericity, the h values, representing total column AOD per unit volume
316 concentration, are computed using the DLS (sphere and spheroid) model (Dubovik et al., 2006) at
317 volume concentration of $1 \mu\text{m}^3/\mu\text{m}^2$. h_f and h_c are computed separately for the fine and coarse
318 modes within the MAIAC look-up table generation package and can be used to assess mass
319 extinction efficiency (MEE) with assumption of particle density. The column-integrated mass
320 concentration of the chemical component is calculated as $C_{M,i} = C_v \cdot f_i \cdot \rho_i$, where i indicates
321 inclusions (BC and BrC) and ρ is mass concentration per unit volume. We use ρ_{BC} of 1.8 g/cm^3
322 and ρ_{BrC} of 1.2 g/cm^3 following previous studies (Bond and Bergstrom, 2006; Turpin and Lim,
323 2001; Schuster et al., 2016; Li et al., 2020).

324 2.3 Study regions

325 We selected two major regions where smoke aerosols are dominant but exhibit different
326 characteristics: North America (170°W - 50°W and 13°N - 80°N) and Central Africa (8°E - 42°E and
327 17°S - 5°N). To avoid potential interference from dust aerosols on smoke analysis, we excluded the
328 Sahel region bounding the Sahara Desert from this study. The selected smoke aerosol analysis
329 regions, along with detected fire counts from the Visible Infrared Imaging Radiometer Suite
330 (VIIRS) instrument onboard the Suomi National Polar-orbiting Partnership (SNPP) satellite in
331 2018, are presented in Fig 2. This study focused on the entire year of 2018, a year marked by one
332 of highest monthly average AOD during the summer over North America (Eck et al., 2023). The
333 EPIC dataset exhibited no temporal gaps, and ample AERONET and CALIOP data were
334 accessible. Additionally, we included a single case study from 2017 to complement our analysis
335 over North America.



336
 337 Figure 2. Cumulative fire detection counts from VIIRS within a 0.1° by 0.1° longitude-latitude
 338 grid in 2018 over North America and Central Africa. The study regions are denoted by grey
 339 rectangles, and AERONET locations are marked with blue stars. Subregions including western
 340 (“NA-West”) and Mexico (“NA-Mexico”) in North America, as well as tropical forest (“CA-
 341 Forest”) and savanna (“CA-Savanna”) regions in Central Africa are denoted by blue rectangles.

342 2.4 AERONET

343 In order to evaluate the EPIC-retrieved AOD and spectral absorption, we utilized the
 344 Version 3 Level 2.0 AERONET Inversion dataset (Holben et al., 1998; Dubovik and King, 2000;

345 Giles et al., 2019; Sinyuk et al., 2020). The EPIC-retrieved AOD_{443} , SSA_{443} and SSA_{680} were
346 compared with the AERONET counterpart derived from direct and sky radiance measurements.
347 The AERONET measurements of spectral AOD have accuracy of ~ 0.01 to 0.02 at optical air mass
348 of one with higher uncertainty in the UV (Eck et al., 1999). The AERONET retrieved SSA at 440
349 nm have uncertainty of ~ 0.03 at $AOD(440)=0.4$ with smaller uncertainties at larger AOD,
350 decreasing to ~ 0.015 at $AOD(440)=1.3$ for biomass burning aerosols at the Mongu, Zambia site
351 (Sinyuk et al., 2020). Spatiotemporal collocation between AERONET and EPIC measurements
352 was conducted as follows: (1) averaging AERONET AOD within a ± 30 -min range and averaging
353 SSA within a ± 3 -hour range from the EPIC measurement time, and (2) averaging EPIC 5×5 pixels
354 ($\sim 50 \times 50 \text{ km}^2$) collocated with the AERONET sites and limited to cosines of solar zenith angle
355 and view zenith angle above 0.45 (i.e., solar zenith angle & view zenith angle $< 63.3^\circ$). The EPIC
356 pixels were spatially averaged when at least 50% of EPIC smoke products are valid in the spatial
357 window. AERONET retrievals with extinction Ångström exponent between 440 and 675 nm
358 greater than 0.4 were selected to avoid possible dust contamination. SSA validation was conducted
359 only when AERONET AOD at 440 nm was greater than 0.6. The AERONET sites with at least
360 five measurements available were considered. Consequently, a total of 28 and 7 AERONET sites
361 were chosen over North America and Central Africa, respectively (see Fig 2).

362 2.5 CALIOP

363 The Cloud-Aerosol Lidar with Orthogonal Polarization (CALIOP) onboard Cloud-Aerosol
364 Lidar and Infrared Pathfinder Satellite Observations (CALIPSO) satellite has provided global
365 measurements of aerosol vertical distribution. We collected profiles of total attenuated backscatter
366 coefficients at 532 nm (β , unit of $\text{km}^{-1}\text{sr}^{-1}$) from the CALIPSO Lidar Level 2 Aerosol Profile
367 version 4.51 dataset (“CAL_LID_L2_05kmAPro-Standard-V4-51”) in 2018. Subsequently, we
368 calculated backscatter-weighted aerosol layer height using the formula $ALH_{\text{CALIOP}} = \frac{\sum \beta z}{\sum \beta}$, where
369 z represents the height of each layer. This definition is widely employed for validating aerosol
370 layer height using CALIOP (Go et al., 2020; Xu et al., 2019). The ALH_{CALIOP} data within a ± 30
371 min from EPIC acquisitions were spatially averaged within MAIAC EPIC grid. We used the same
372 cutoff threshold for the Sun and view zenith angle as above. To mitigate ALH uncertainty for weak
373 aerosol cases, the ALH comparison was conducted when CALIOP AOD at 532 nm exceeded 0.6.

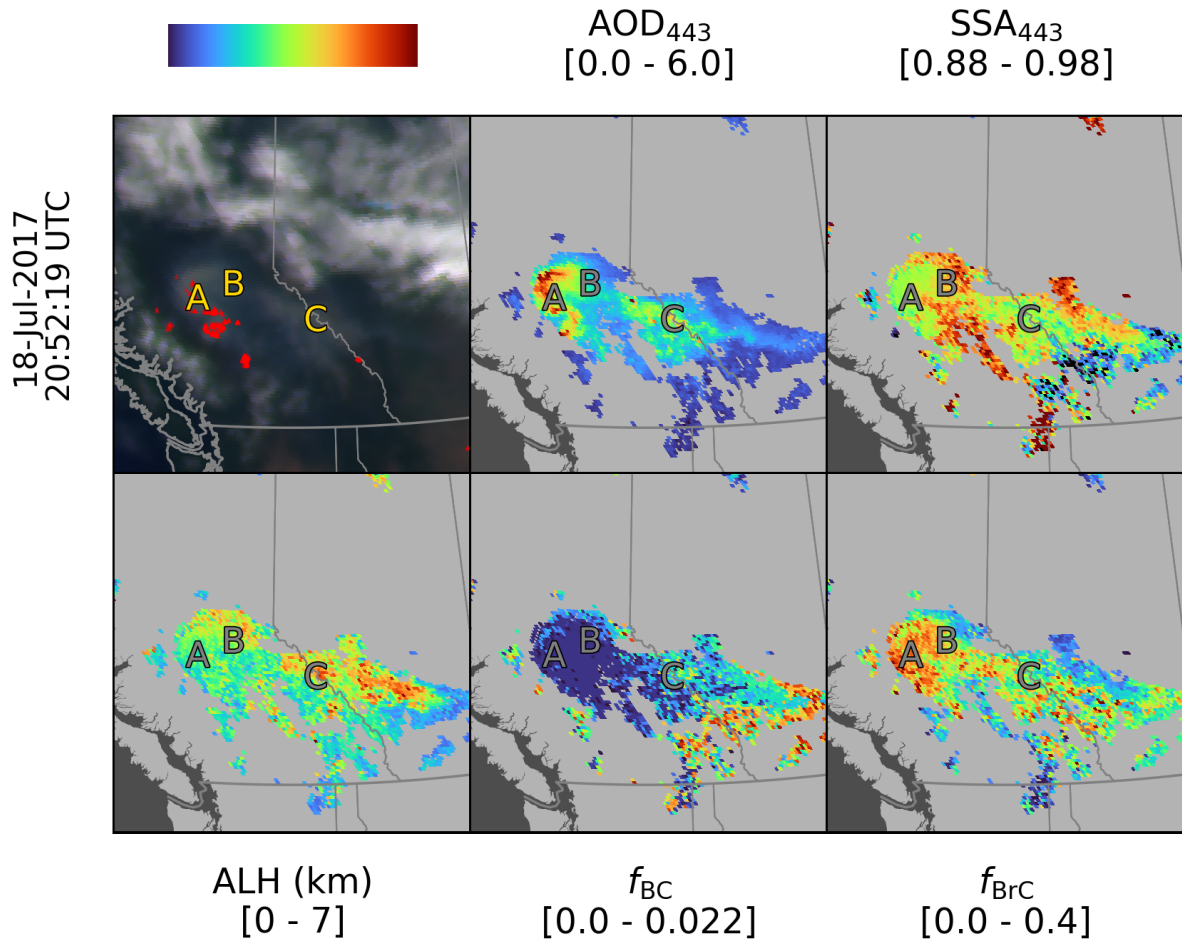
374 3. Results

375 3.1 Analysis of individual cases

376 3.1.1 North America

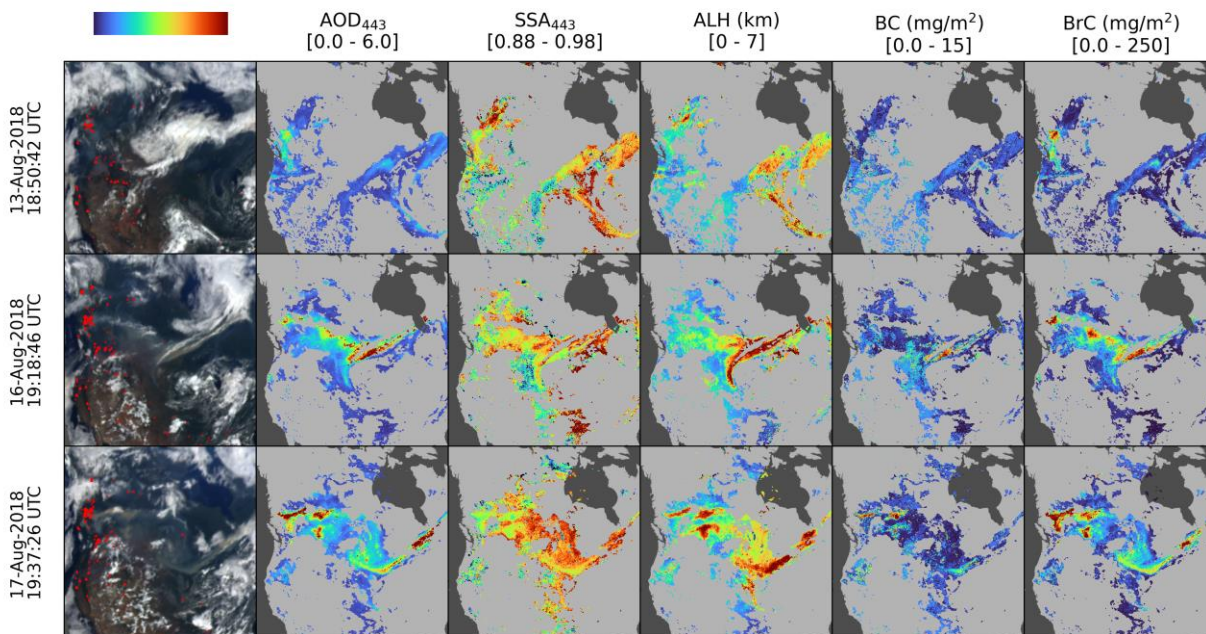
377 Western North America stands out as one of the most active wildfire regions globally. For
378 our analysis, we selected an intense wildfire and associated smoke aerosol event occurring on July
379 18, 2017, at 20:52:19 Coordinated Universal Time (UTC) over western Canada in Fig 3. Note that

380 all other analyses in this study are for 2018 except for this case. Utilizing the VIIRS/SNPP Thermal
381 Anomalies/Fire (Schroeder and Giglio, 2018), visualized as red dots within the true-color images,
382 we identified wildfires in British Columbia. The true-color image and retrieved smoke particle
383 properties illustrate the eastward transport of the smoke plume. Specifically, pixels near the
384 wildfires (region “A” in Fig 3) exhibited AOD_{443} nearing ~4-6, alongside an SSA_{443} of ~0.93.
385 Pixels approximately 50~100 km from the sources (region “B”), show decreased AOD_{443} (~2) and
386 less absorption (SSA_{443} of ~0.96). Notably, the contrast in SSA is more pronounced at 388 nm
387 than at 680 nm (not shown). Absorption changes within this distance are related to the aging
388 process. Freshly emitted particles from wildfires exist in various mixing states and undergo
389 multiple processes, such as coagulation, condensation/evaporation, oxidation, and secondary
390 aerosol particles formed from chemical production (Reid et al., 2005a, b; Liu et al., 2020). Smoke
391 aerosol mixtures become less absorbing in the UV and shortwave visible wavelengths when
392 transported from sources through these aging processes, consistent with findings from other *in-*
393 *situ* and remote sensing measurement studies (Junghenn Noyes et al., 2020a, b; Kleinman et al.,
394 2020). The increased SSA_{443} from 0.93 to 0.96 (from region “A” to “B”) corresponds to a decrease
395 in the BrC fraction from 0.3 to 0.1. Aerosol plumes over Alberta, farther downwind to the east
396 (region “C”), exhibited a) high AOD_{443} values (1-3), b) SSA_{443} of ~0.92-0.94, c) increased BC
397 volume fraction up to 0.01; and d) a similar BrC volume fraction (about 0.3 at the plume center)
398 for pixels close to the fire sources. The eastern part of the plumes was located farther away from
399 the source and could have undergone more extensive aging. Smoke aerosol near sources was
400 located close to the surface (ALH above sea level of ~1 km) and was elevated to about 5-6 km in
401 the downwind area. It is important to consider that the fires could also undergo various stages of
402 combustion intensity over time, which could also be a factor in BC and BrC production. The
403 observed differences in ALH suggest that possibly some of these fires were more intense earlier,
404 leading to the lofting of the plume to 5-6 km. Subsequently, the intensity may have decreased,
405 resulting in a lower ALH as the plume transitioned to a more smoldering phase. This scenario,
406 particularly applicable to long plume lengths, implies that fire intensity and the relative combustion
407 fraction (flaming/smoldering) likely varied over the course of several hours during the transport
408 of such a long plume distance.



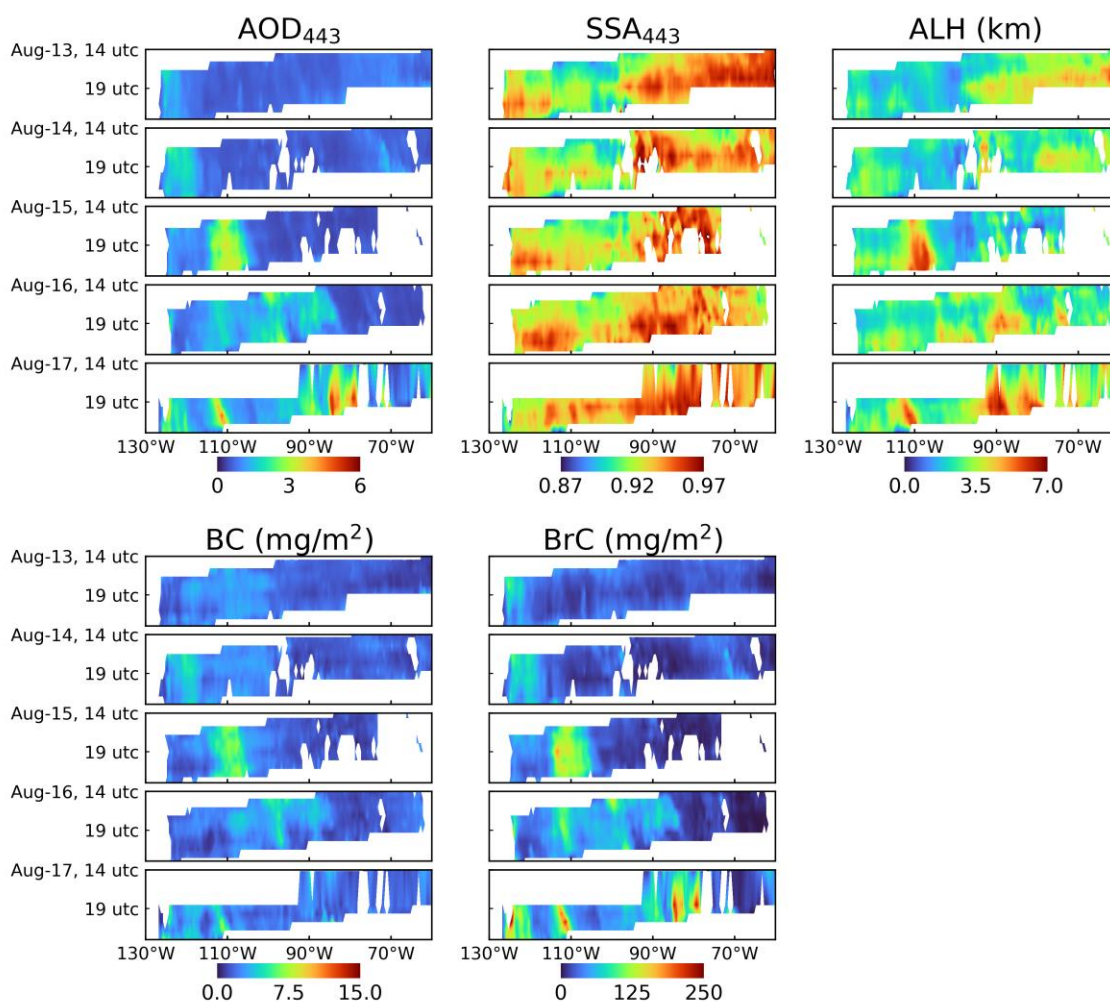
409
 410 Figure 3. Illustration of EPIC smoke aerosol optical properties over western North America on
 411 July 18, 2017. Red dots in the first left panel are VIIRS/NPP thermal anomaly hotspots. The
 412 underlying image and analyses in subsequent panels correspond to EPIC true color and MAIAC
 413 EPIC retrievals (AOD_{443} , SSA_{443} , and ALH) with inferred BC and BrC volume fractions. The color
 414 bar scale is indicated at the top of each panel.

415
 416 Continental-scale smoke aerosol episodes in August 2018, derived from the analysis of
 417 Lyapustin et al. (2021b), are depicted in Fig 4. On August 13 (top panels), smoke aerosol plumes
 418 along the west coast of North America, near the detected wildfire sources, exhibit high AOD of
 419 nearly 3-4 and SSA_{443} of 0.93 in the plume center. Surrounding pixels of the plume generally show
 420 lower AOD and higher SSA than the pixels interior to the plume. Subsequently, westerly
 421 transported plumes with increased AOD (up to ~6) and ALH (~6-7 km) were detected on August
 422 16 and 17. Corresponding BC and BrC fractions ranged from 0.005 to 0.01 and 0.2 to 0.3 (not
 423 shown), with column mass concentrations reaching 15 mg/m² and 250 mg/m², respectively.



424
 425 Figure 4. Illustration of smoke aerosol optical properties (AOD₄₄₃, SSA₄₄₃, ALH, and BC and BrC
 426 mass concentrations) over North America on August 13, 16, and 17, 2018. The color bar scale is
 427 indicated at the top of each panel.

428
 429 EPIC can effectively monitor the changeregional-to-continental scale variability of smoke
 430 optical properties during transport at high temporal cadence. Meridional averages of AOD₄₄₃,
 431 SSA₄₄₃, ALH, and BC and BrC mass concentrations over the period from August 13 to 17, 2018
 432 are represented as Hovmöller diagrams in Fig 5. Plume evolution is clearly captured, with a
 433 temporal resolution of 1-2 hours, from initial smoke aerosol emission over western North America,
 434 to subsequent transport toward the east with an increased ALH from ~1 km to 6-7 km, and
 435 eventually to dispersion.

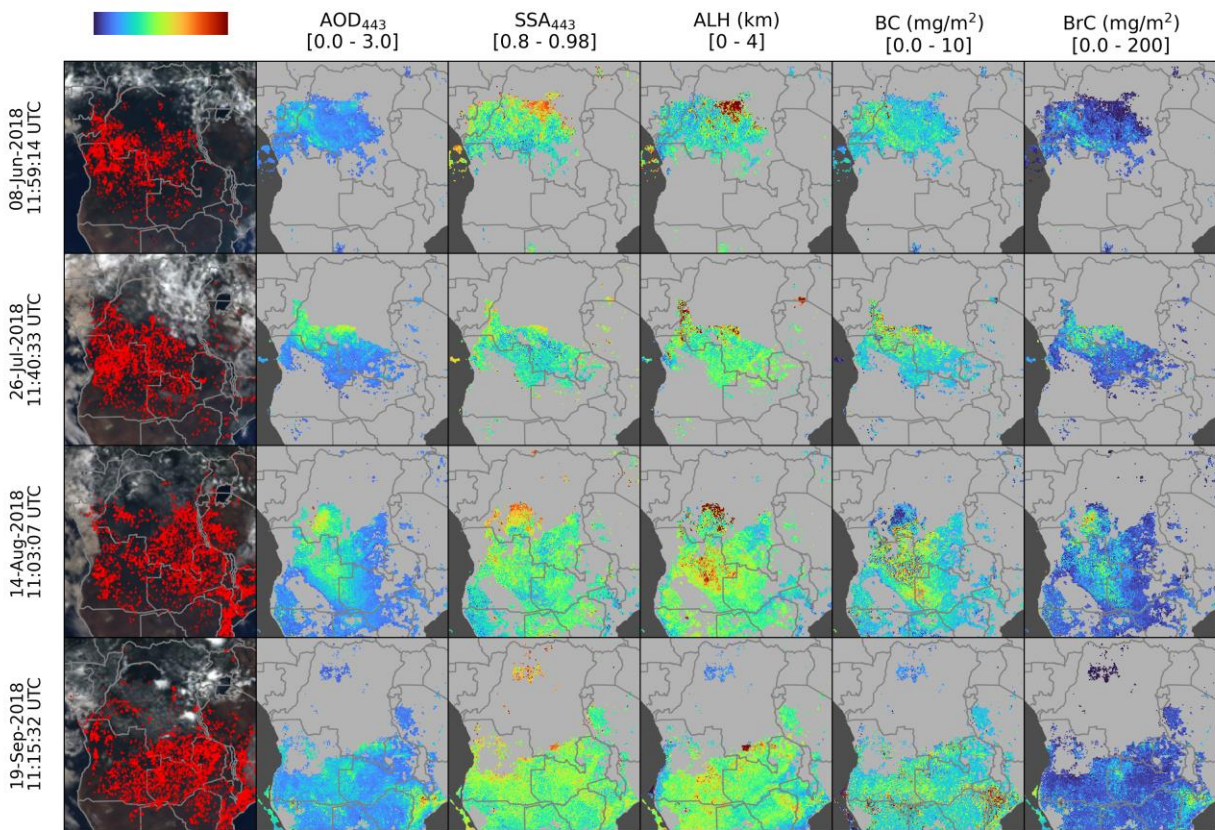


436
 437 Figure 5. Hovmöller diagrams of AOD₄₄₃, SSA₄₄₃, ALH, and BC and BrC volume fractions over
 438 North America (130-60°W, 25-53°N, 0.5° longitudinal interval) from August 13 to 17, 2018. Gaps
 439 in the data are due to low AOD or meteorological clouds.

440 3.1.2 Central Africa

441 Biomass burning over Central Africa generates smoke aerosols with distinct optical
 442 properties. Long-term AERONET measurements over Southern Africa savanna regions indicate
 443 the strongest absorption among global smoke regions, with SSA values at 440 and 680 nm of 0.87
 444 and 0.86, respectively (Dubovik et al., 2002; Giles et al., 2012; Sayer et al., 2014). The biomass
 445 burning emission pattern in Africa follows a clearly defined seasonal cycle, influenced by
 446 precipitation linked to the seasonal movement of the Inter-Tropical Convergence Zone (ITCZ)
 447 (Swap et al., 2003). There exists a strong temporal cycle of SSA as well, with the lowest SSA
 448 values in June due to savanna burning, and increasing through October as more forested areas burn

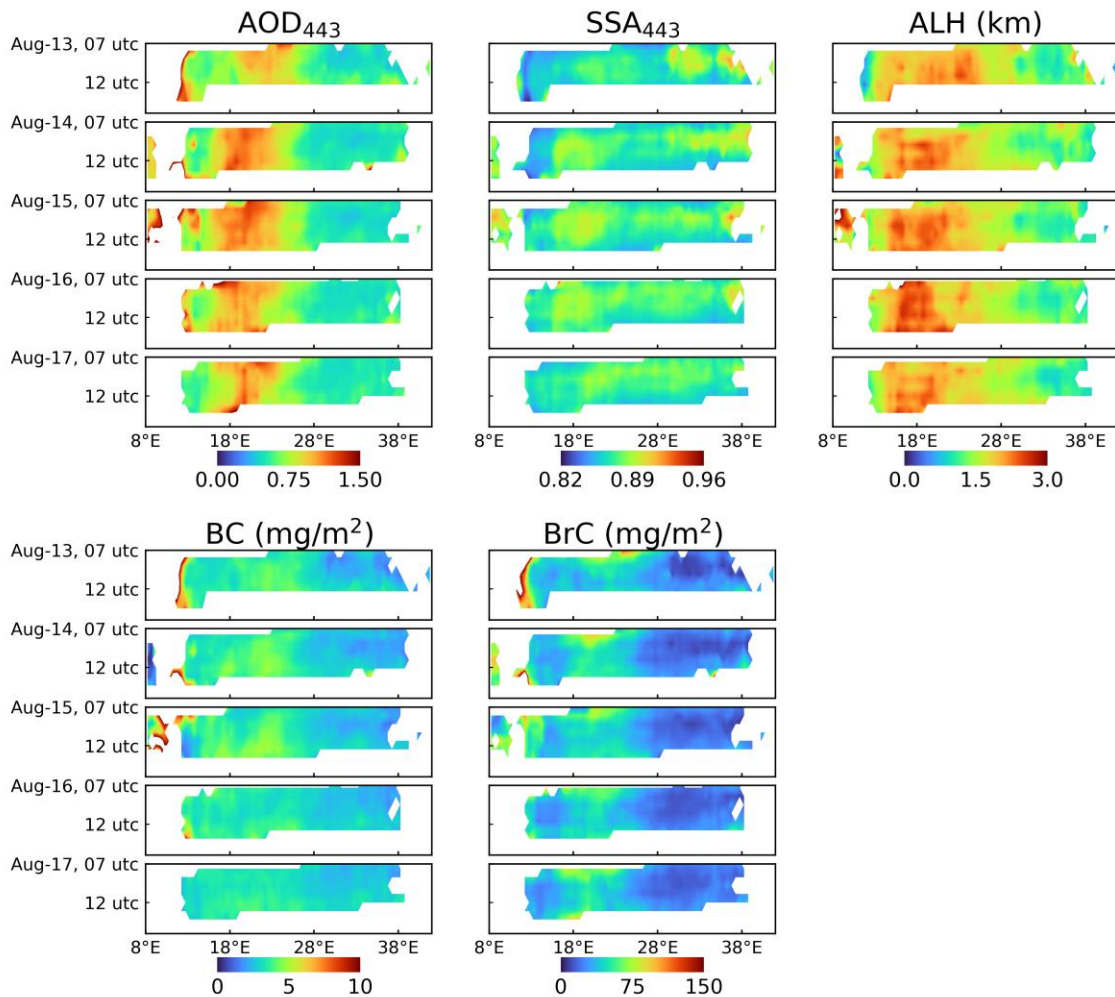
449 (Eck et al., 2013). And yet, particle size distributions tend to remain unchanged (Reid et al., 2005b;
 450 Sayer et al., 2014). This makes the region an ideal test environment for absorption retrievals. We
 451 selected four cases (June 8, July 26, August 14, and September 19, 2018) to illustrate the seasonal
 452 changes in smoke regions from northeast to southwest; these align closely with the climatological
 453 patterns detected by other ground-based and satellite measurements (Eck et al., 2013; Duncan et
 454 al., 2003). The detected fires were subcontinent-wide (Fig 6) and generated smoke with AOD
 455 reaching up to ~ 2 . The general particle properties were consistent across the four cases. The light
 456 absorption, reaching as low as ~ 0.84 SSA_{443} , was notably stronger than in the cases over North
 457 America. The ALH of pixels with high AOD remained relatively constant at 2-3 km. High BC
 458 concentrations (e.g., > 5 mg/m^2) were prevalent over detected fire locations despite relatively
 459 lower AOD condition (e.g., $AOD_{443} < 2$) than in the cases over North America, where similar BC
 460 concentrations were observed from the pixels with $AOD_{443} > \sim 3$.
 461



462
 463 Figure 6. Illustration of smoke optical properties (AOD_{443} , SSA_{443} , ALH, and BC and BrC mass
 464 concentrations) over Central Africa on June 8, July 26, August 14, and September 19, 2018.
 465

466 The measurements taken over five consecutive days from August 13-17 over the Central
 467 Africa study region detected weaker zonal smoke plume transport with less dynamic changes in
 468 particle properties (Fig 7) compared to the North America cases (Fig 5). The relatively low ALH

469 of 2-3 km indicates that smoke aerosol mostly concentrated within the boundary layer and was
 470 less influenced by strong jets at higher altitudes. AOD was slightly enhanced during early morning
 471 and late afternoon by ~10-20% over 20-25°E region. The afternoon pattern is consistent with long-
 472 term AERONET measurements shown in Eck et al. (2003), whereas the morning pattern should
 473 be further analyzed. From SEVIRI measurements, the peak of active fires is most frequently
 474 detected around noon (Wooster et al., 2021). Eck et al. (2003) concluded that elevated air
 475 temperatures, reduced relative humidity, and heightened wind speeds during the midday and
 476 afternoon periods often lead to more intense and rapidly spreading fires.



477
 478 Figure 7. Same with Fig 5 except for over Central Africa (8-42°E, 17°S-5°N, 0.5° longitudinal
 479 interval) from 13 to 17 August 2018.

480
 481 The observed difference between the two regions clearly correlates with the different fuel
 482 types – forests in North America and savannah grasses and bushes in Central Africa. For instance,

483 forest wildfires in North America with much higher thermal energy density result in elevated ALH,
484 incomplete combustion, and higher BrC concentrations, whereas fast-spreading grassland fires are
485 known for high BC concentration from flaming combustion emissions, but lower energy density,
486 which keep generated smoke generally within the boundary layer over Central Africa.

487 High fuel consumption can explain higher ALH from North America with more thermal
488 energy. Fuel consumption is defined as the amount of biomass, coarse and fine litter, and soil
489 organic matter consumed per unit area burned. It is the product of fuel load and combustion
490 completeness, leading to regional differences. For instance, western US, Canada, and Siberia
491 regions categorized as boreal forests exhibit high fuel consumption (e.g., > 2 kg C m⁻² burned),
492 whereas the savanna region in Central Africa has lower fuel consumption (e.g., 1–2 kg C m⁻²
493 burned; van der Werf et al., 2017). The energy released along the flame front is directly related to
494 plume height, with plumes from these fires reaching altitudes between 2.2 km and 13 km (Lavoué
495 et al., 2000). Satellite-derived fire radiative power also shows significant differences between
496 smoke plumes in the free troposphere (1620–1640 MW) and those within the boundary layer
497 (174–465 MW; van der Werf et al., 2010).

498 **3.2 Comparison of smoke properties derived from AERONET and CALIOP**

499 The regional validation of AOD, spectral SSA, and ALH throughout 2018 using the
500 AERONET and CALIOP datasets is presented in Fig 8. The AOD comparison over North America
501 demonstrates a correlation coefficient (R) of 0.91 and a root mean squared error ($rmse$) of 0.22. It
502 is important to note that this comparison only covers smoke retrievals; it excludes low AOD
503 conditions (e.g., background AOD at 443 nm < 0.4), that may result in lower validation statistics
504 compared to the previous analysis incorporating the combined “background+smoke” AOD (R of
505 0.85 and $rmse$ of 0.13 in Lyapustin et al., 2021b). Nonetheless, the mean bias error (MBE) of 0.02
506 in version 3 is smaller than the 0.05 reported by Lyapustin et al. (2021b) based on v2. ~~The~~
507 ~~fraction~~ 74.9% of results fall within the expected error ($EE\%$), envelope for AOD, defined as
508 $\pm(0.05+0.2\times\text{AERONET AOD})$, is 74.9%.) from AERONET AOD. Hereafter, “ EE ” refers to a
509 percentage of retrievals within the expected error envelope. Central Africa AOD also exhibits
510 similar validation statistics, except for a lower R (0.60), likely due to a narrow range of collocated
511 AOD compared to North America. However, the MBE of -0.04 and $EE\%$ of 74.8% are comparable
512 to the statistics for North America. Despite the absence of IR channels for cloud detection and the
513 relatively coarse spatial resolution (>10 km) of EPIC, which can lead to sub-pixel cloud
514 contamination (Marshak et al., 2018), the achieved accuracy in AOD retrieval is very encouraging.

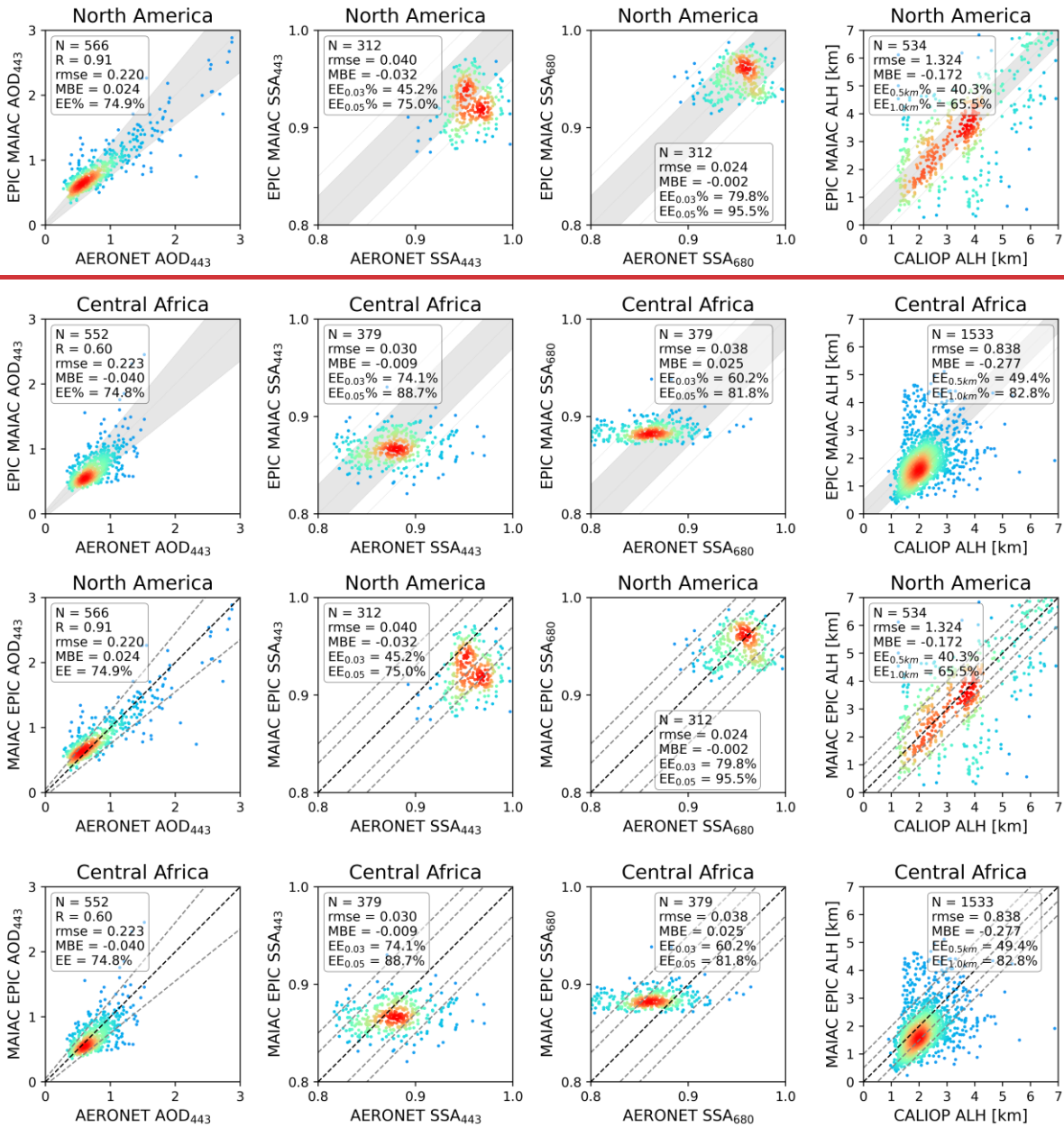
515 Regional comparisons of SSA with AERONET retrievals are more distinct than those of
516 AOD. Overall, the SSA_{443} over North America from EPIC is lower than that from AERONET with
517 MBE of -0.03 and ~~EE fraction ($EE_{0.03}$ for SSA, defined as a percentage of retrievals~~ within ± 0.03
518 ~~+from AERONET SSA; $EE_{0.03}\%$) of,~~ is 45.2%. The collocated range spans about 0.88 to 0.97
519 from EPIC and 0.90–1.00 from AERONET. Comparisons over Central Africa show a much smaller
520 bias (MBE of -0.01) and higher $EE_{0.03}\%$ of 74.1%. The regional difference in accuracy could be
521 attributed to uncertainty in our assumptions of regional smoke model properties (e.g., particle size

522 and real refractive index). Nonetheless, the retrieved MAIAC EPIC SSA₄₄₃ remains comparable
523 to OMAERUV SSA₄₄₀ retrievals (*rmse* of 0.04 and *EE*_{0.03%} of 57.5% over North America; *rmse*
524 of 0.04 and *EE*_{0.03%} of 66.4% over South America and Southern Africa in Jethva et al., 2014) and
525 TropOMAER SSA₄₄₀ retrievals (*rmse* of 0.04 to 0.04; *EE*_{0.03%} of 48 to 51% in Torres et al., 2020).
526 Additionally, it is worth noting that the current AERONET algorithm has a strong spectral
527 smoothness constraint for the imaginary part of refractive indices, resulting in less representation
528 of BrC (Sinyuk et al., 2022; Eck et al., 2023). By employing the relaxed constraint, they found
529 decreased SSA (e.g., more absorbing) with smaller sky radiance error from wildfire cases
530 containing a large amount of BrC. However for the biomass burning cases shown in Sinyuk et al.
531 (2022) for both North America wildfire smoke and savanna burning smoke in Zambia the
532 difference in spectral SSA at 443 nm were ~0.01 or less for the relaxed versus standard V3
533 constraints, while some differences in SSA at 675 nm were ~0.02 for North American smoke only.
534 With this update from the AERONET side, we anticipate a potentially better agreement between
535 EPIC and AERONET for SSA₄₄₃ and possibly better for SSA₆₈₀ in the future.

536 SSA₆₈₀ retrievals from North America show better agreement with AERONET than SSA₄₄₃
537 with a smaller *MBE* of -0.002, *rmse* of 0.02, and higher *EE*_{0.03%} (79.8%). However, Central Africa
538 shows slightly less agreement in SSA₆₈₀ compared to SSA₄₄₃, with a higher positive bias (*MBE* of
539 0.03) and smaller *EE*_{0.03%} of 60.2%. Additionally, the retrieved range of SSA₆₈₀ is relatively
540 narrower (~0.87 to 0.92) than that of AERONET (~0.80 to 0.99). Regardless, the statistics metrics
541 are much closer to POLDER GRASP SSA₆₈₀ retrievals (*rmse* of 0.06; *MBE* of -0.04 to -0.02 in
542 Chen et al., 2020).

543 The comparison of EPIC ALH with CALIOP also reveals strong regional dependence.
544 Most collocated ALH retrievals are relatively high over North America (3-4 km) and sometimes
545 reach 6-7 km. In Central Africa, ALH ranges from 0 to 4-5 km, with most collocated retrievals
546 falling within 1-3 km. The *rmse* value is closely related to the range of ALH; thus, it is relatively
547 high in North America (1.32 km). More favorable validation statistics were extracted from Central
548 Africa (*rmse* of 0.84 km; *EE*_{0.5km} of 49.4%; *MBE* of -0.28 km), where *EE*_{0.5km} is a percentage of
549 retrievals within a range of ± 0.5 km from CALIOP ALH. This level of accuracy, derived from
550 long-term validation rather than selected individual cases, is better than the operational TROPOMI
551 ALH (*MBE* of -2.41 to -1.03 km and *rmse* of 1.97-3.56 km in Nanda et al., 2020).

552



553

554

555

556

557

558

559

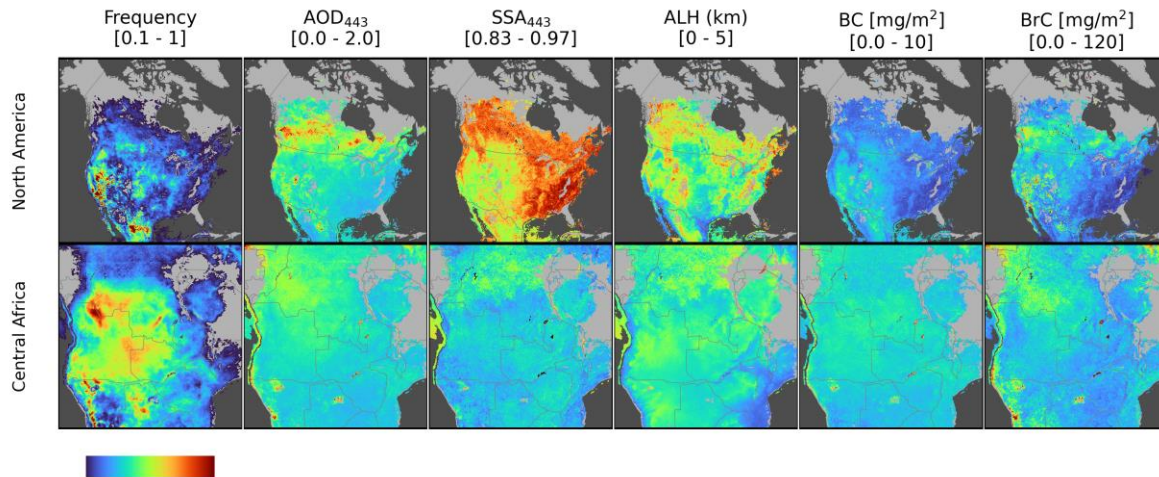
560

561

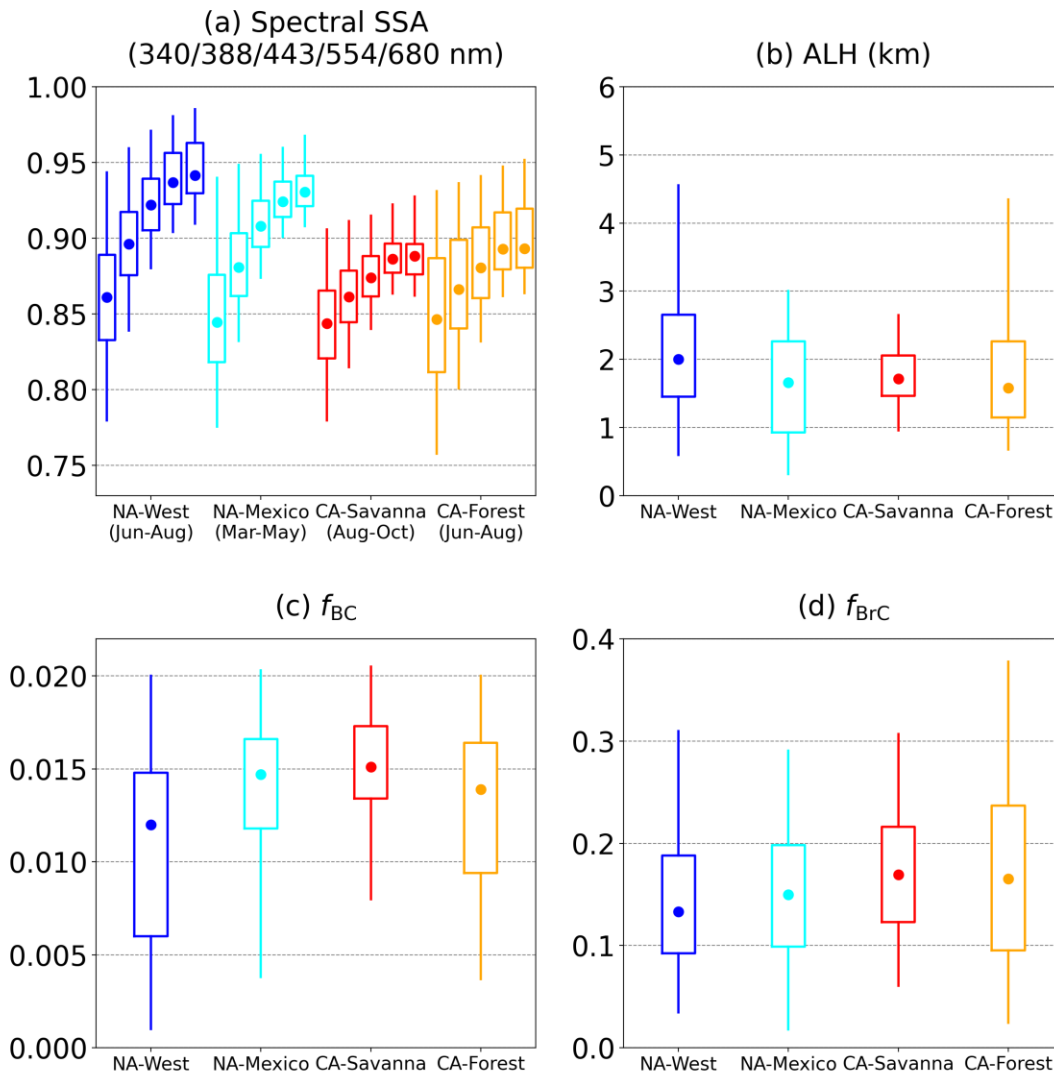
Figure 8. Comparison of MAIAC EPIC smoke AOD₄₄₃ (first column), SSA₄₄₃ (second column), SSA₆₈₀ (third column) with AERONET, and ALH with CALIOP (fourth column). Color represents the relative frequency of retrievals. The black dashed lines are 1:1 reference line. The gray dashed lines and shaded areas are the 1:1 reference line and are ranges of expected error envelopes: $\pm (0.05 + 0.2 \times \text{AERONET AOD})$; $\pm (\text{AERONET SSA} + \text{AOD})$; ± 0.03 or $\pm (\text{AERONET SSA} + 0.05)$; from AERONET SSA; and $\pm (\text{CALIOP ALH} + 0.5 \text{ km})$ or $\pm (\text{CALIOP ALH} + 1.0 \text{ km})$; from CALIOP ALH.

562 **3.3 Regional climatology of smoke properties**

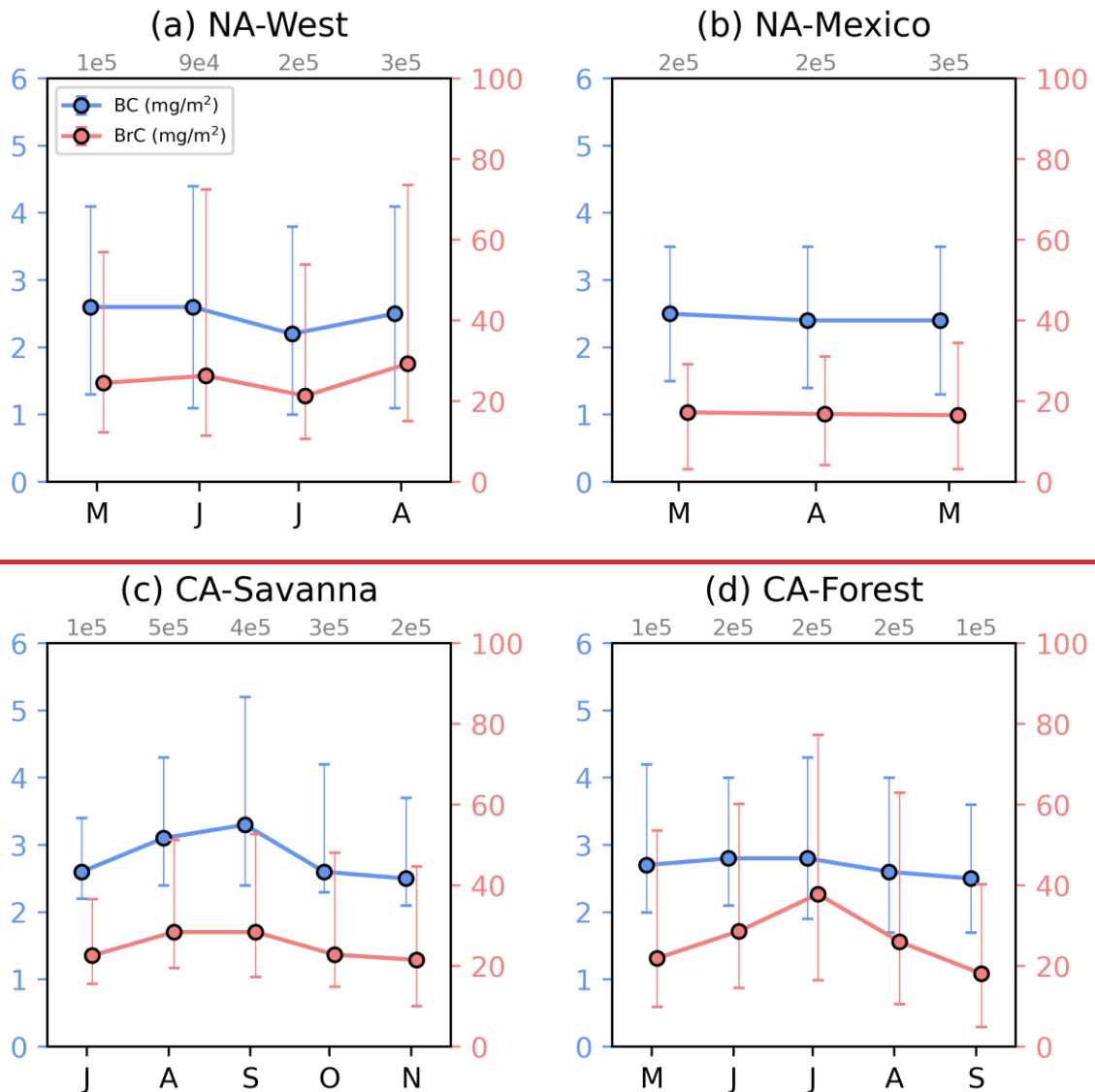
563 We compiled all the smoke properties retrieved for 2018 and conducted a regional analysis
564 to understand their climatology and relationships with environmental factors such as vegetation
565 and fuel type, as well as meteorological conditions. Regional geographical distributions are
566 illustrated in Fig 9, and the corresponding statistical distributions are presented as box-whisker
567 plots in Fig 10. ~~Regional and monthly averaged BC and BrC mass concentrations are presented~~
568 ~~in Fig 11.~~
569



570
571 Figure 9. Spatial distribution of relative retrieval frequency (i.e., relative number of retrievals) and
572 smoke properties (AOD₄₄₃, SSA₄₄₃, ALH, and BC and BrC mass concentrations) for 2018 over
573 North America (top panels) and Central Africa (bottom panels). Pixels with retrieval frequencies
574 lower than 10% compared to the regional maximum are filtered out. The color bar scale is indicated
575 at the top of each panel.



576
 577 Figure 10. Distribution of (a) spectral SSA, (b) ALH, (c) BC volume fraction, and (d) BrC volume
 578 fraction over western North America (“NA-West”) and Mexico (“NA-Mexico”) in North America,
 579 and savanna (“CA-Savanna”) and tropical forest (“CA-Forest”) in Central Africa. Whiskers give
 580 the 5th and 95th percentiles; boxes represent the 25 and 75th percentiles; and dots denote the 50th
 581 percentile. In (a), five consecutive box-whisker plots for each region represent different
 582 wavelengths (340, 388, 443, 554, and 680 nm from left to right).
 583



584
 585 **Figure 11. Regional monthly BC and BrC mass concentrations over western North America (“NA-**
 586 **West”) and Mexico (“NA-Mexico”) in North America, and savanna (“CA-Savanna”) and tropical**
 587 **forest (“CA-Forest”) regions in Central Africa. Whiskers denote the 15.9th and 84.1st percentiles;**
 588 **dots denote the 50th percentile. The number of smoke retrievals is displayed in grey at the top of**
 589 **each panel.**

590
 591 Active wildfires occur in late spring and summer over western North America, with
 592 expanded burned areas over the years (Dennison et al., 2014; Kalashnikova et al., 2018; Liu et al.,
 593 2010). Most smoke retrievals were detected over the western United States (e.g., California,
 594 Oregon, Washington) and western Canada (e.g., British Columbia) (Fig 9). The optical properties
 595 were quite distinct between source regions and downwind regions. The western US and western

596 Canada source regions show relatively low SSA and ALH, while central Canada, which is a source
597 region, but also mostly downwind regions for transported heavy smoke plume from western
598 regions, show higher SSA and ALH. This difference is closely related to the smoke aging process
599 discussed in Sec 3.1.1. Spatiotemporally integrated spectral SSA over western North America
600 (“NA-West” region in Fig 2) of 0.86, 0.89, 0.92, 0.94, and 0.95 at 340, 388, 443, 554, and 680 nm,
601 respectively, align with the range 0.915-0.935 at 443 nm and 0.95-0.97 at 680 nm derived from
602 multiple AERONET measurements in September 2020 (Eck et al., 2023). The mean and standard
603 deviation of ALH was 2.2 ± 1.2 km with a wide range of values up to 4.6 km at the 95th percentile
604 (Fig 10b). The mean BC volume fraction of 0.011 ± 0.006 was the lowest among the selected
605 regions. The number of smoke pixels was maximum in August, with the highest BrC mass
606 concentration (median value of 29 mg/m^2), synchronized with seasonal wildfire activities over
607 western North America. Although BC and BrC concentrations can reach up to more than 5 mg/m^2
608 and 100 mg/m^2 , respectively, over some specific regions (Fig 9), the averaged values were not as
609 high due to high spatiotemporal variation (Fig 11a). Another smoke-dominated region in North
610 America is found over Mexico (“NA-Mexico” region in Fig 2), where both natural wildfires and
611 agricultural burns occur annually during the hot and dry season (March to May; Rios et al., 2023).
612 This region exhibited smoke properties with more absorption and lower ALH with lower variation
613 (1.6 ± 0.9 km) than western US.

614 Central Africa is climatologically the largest global biomass burning source, peaking
615 during the austral winter. The region contributes approximately one-third of Earth’s biomass
616 burning emissions from various sources, including wildfires, agricultural fires, and industrial
617 activities (van der Werf et al., 2010). The distribution of smoke retrievals appears relatively
618 homogeneous and similar to that of detected fires, with widespread retrieval frequency in Angola,
619 Democratic Republic of the Congo, and Zambia, and more varied sources in Namibia (Fig 9).
620 During the August–October burning season in Central Africa, aerosol light-absorption is
621 predominantly attributed to BC, a byproduct of savanna burning characterized by significant
622 flaming-phase combustion (Ward et al., 1996). Although the retrieved smoke AOD is not as high
623 as in North America, light absorption over savanna region in Central Africa (“CA-Savanna” region
624 in Fig 2) was more substantial, leading to higher BC and BrC mass concentrations. Low SSA
625 spanned from UV through the visible (0.84, 0.86, 0.88, 0.89, and 0.89 at 340, 388, 443, 554, and
626 680 nm, respectively), with higher BC and BrC volume fractions of 0.015 and 0.178, respectively.
627 The ALH is lower and less variance (1.8 ± 0.6 km; 2.6 km for the 95th percentile) that of western
628 North America. The BC and BrC mass concentrations increased from July, peaked in September
629 (median values of 3.3 mg/m^2 and 28.4 mg/m^2 , respectively), and declined toward November (Fig
630 11e); this aligns with long-term AERONET AOD measurements (Eck et al., 2003) and with
631 AERONET-based BC and BrC estimations (Schuster et al., 2016). By contrast, smoke from
632 tropical forest fires in Central Africa (“CA-Forest” region in Fig 2) shows slightly less absorption
633 with lower BC volume fraction (0.013) and larger variabilities of BrC volume fraction ($0.018 \pm$
634 0.11) and ALH (1.9 ± 1.1 km) than that of savanna region. BC and BrC mass concentrations over

635 the tropical forest region in Central Africa peak in July (earlier than savanna region) with lower
636 BC (2.8 mg/m^2) and higher BrC (37.8 mg/m^2 ; Fig 11d) than those of the savanna region.

637 4. Discussions

638 4.1 Comparison of the BrC to BC mass concentration ratio with other studies

639 The ratio between OC and EC (OC/EC) is widely used to elucidate the apportionment of
640 carbonaceous components in smoke particles as a proxy for assessing the dominance of primary
641 emissions from flaming combustion (e.g., fossil fuel) versus smoldering combustion emissions
642 and secondary formation of OC (e.g., biomass burning, wildfires, secondary organic aerosol (SOA)
643 formation) (Lim and Turpin, 2002; Pokhrel et al., 2016). As BrC is an absorbing OC among total
644 OC, we inferred regional BrC-to-BC column mass concentration ratios (BrC/BC) from EPIC and
645 compared them with those from other studies providing BrC/BC or OC/EC.

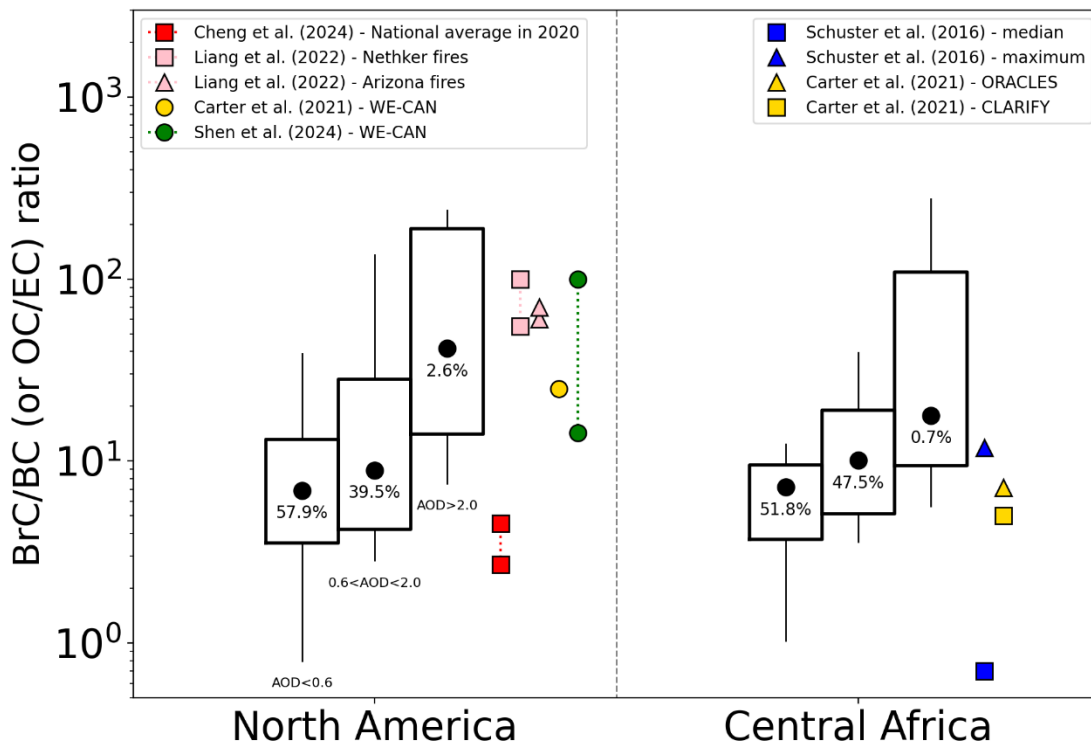
646 Results of BrC/BC ratio from this study in North America and Central Africa are compared
647 with other previous studies in Fig 11. The absolute BC and BrC volume fractions in Central
648 Africa were higher than in North America, resulting in similar median values of the BrC/BC mass
649 concentration ratio (7.3 for North America and 8.0 for Central Africa). When the ratios are
650 categorized into different AOD ranges, the BrC/BC increases with AOD from both regions. For
651 two groups of $\text{AOD} < 0.6$ (“low-moderate AOD”) and $0.6 < \text{AOD} < 2.0$ (“high AOD”), the median
652 BrC/BC is higher in Central Africa (7.2 and 10.1) than in North America (6.9 and 8.9). The
653 variance, represented as the range of estimations, is more significant in North America for the two
654 groups, which could be ascribed to more diverse fuel types from natural, residential, and
655 agricultural sources and related emission processes (Xiong et al., 2022). For the cases of $\text{AOD} >$
656 2.0 (“extremely high AOD”), which corresponds to 2.6% and 0.7% of the entire retrieval record
657 in North America and Central Africa, respectively, North America showed a higher BrC/BC ratio
658 (median value of 41.5) with a higher variance than Central Africa (median value of 17.7). This
659 higher BrC/BC ratio in North America, compared to Central Africa, may have its origin in more
660 common smoldering combustion and/or more SOA formation during transport. Most “extremely
661 high AOD” cases were observed from transport plumes, where the increased BrC/BC ratio is
662 associated with their aging processes including SOA formation. These results are consistent with
663 POLDER/GRASP and MISR aerosol components analysis (Li et al., 2022; Junghenn Noyes et al.,
664 2022).

665 Our estimates exhibit relatively high variance because they encompassed all pixels detected
666 as smoke in the retrieval algorithm over the continents in 2018, rather than being limited to selected
667 heavy plumes. The national average of OC/EC ratio (3.6 ± 0.9) obtained from U.S. EPA ground-
668 based chemical composition measurement networks (including CSN and IMPROVE) for all
669 sources, not only for smoke sources, (Cheng et al., 2024) falls within the estimates from EPIC’s
670 “low-moderate AOD” group. OC/EC ratios obtained from specific wildfire samples including WE-
671 CAN campaign during 2018 July-September over western US (Liang et al., 2022; Carter et al.,
672 2021) range from approximately 14 to 100, corresponding to the “extremely high AOD” group. It

673 is important to note that although the BrC/BC ratio is smaller than the OC/EC ratio, obtaining an
 674 accurate BrC/BC is challenging without proper measurements separating BrC from OC, which is
 675 rarely done in experiments.

676 The ORACLES (August–September 2016) and CLARIFY (August 2017) campaigns over
 677 the eastern South Atlantic Ocean (Carter et al., 2021) measured transported smoke aerosols from
 678 Central Africa. The general level of AOD at 550 nm for both campaigns was ~0.3 to ~0.7
 679 (Haywood et al., 2021; Sayer et al., 2019), and corresponding OC/EC ratios were 5-7, which are
 680 consistent with the estimated EPIC ranges for “low-moderate AOD” and “high AOD”. Another
 681 comparison can be made with the BrC/BC mass concentration ratio inferred from AERONET
 682 measurements (Schuster et al., 2016). Although the definition is similar to ours, both using
 683 column-integrated and remote-sensing-based values, it shows relatively lower values than ours.
 684 This difference could be attributable to the different wavelengths (i.e., UV-Vis for EPIC, Vis-NIR
 685 for AERONET) used for the measurements and different assumptions in the components (e.g.,
 686 dependence of composition on particle size in Schuster et al., 2016).

687 The EPIC BrC/BC ratios increased with AOD, representing aging processes during
 688 transport over North America and Central Africa. They are generally consistent with other studies
 689 despite different measurement characteristics, such as OC/EC vs. BrC/BC, and *in-situ* versus
 690 remote sensing.



691

692 Fig 1211. Regional EPIC-derived BrC to BC column mass concentration ratios across three AOD
693 ranges (AOD < 0.6, 0.6 < AOD < 2.0, and AOD > 2.0). Each box-whisker plot comprises the 5th,
694 15.9th, 50th, 84.1st, and 95th percentiles. The percentages of retrievals per each AOD range are
695 denoted within the box. On the right side of each region panel, the values (or range) of the BrC-
696 to-BC ratio (only for Schuster et al., 2016) or OC-to-BC ratio (all others) from other studies are
697 shown.

698 4.2 Uncertainty of volume fractions due to assumed BC and BrC refractive indices

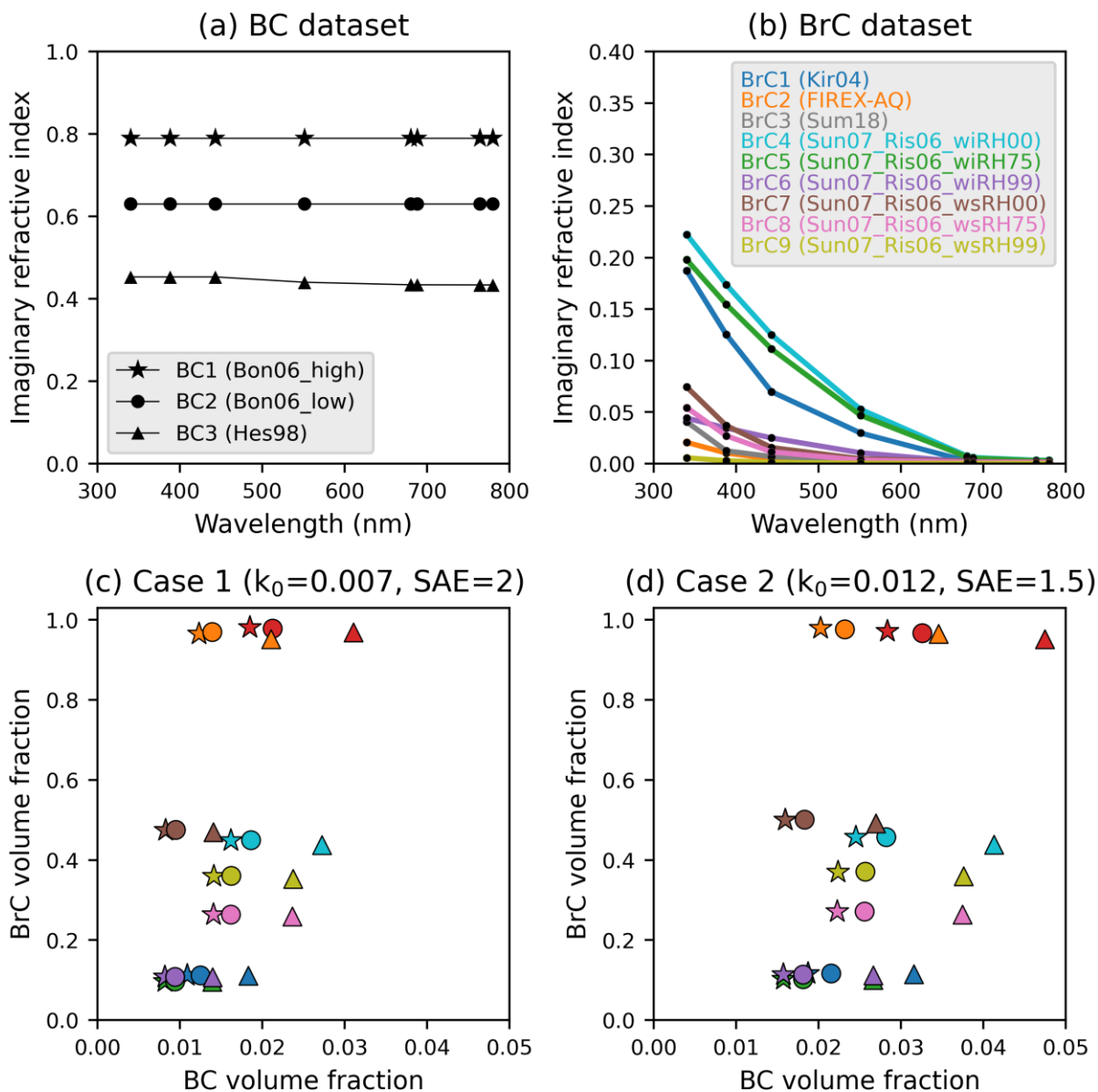
699 Assumed spectral imaginary refractive indices of BC and BrC determine their inferred
700 volume fractions. Identical spectral absorption can result in lower BC and BrC fractions with
701 higher BC and BrC imaginary refractive indices and vice versa. As most satellite measurements,
702 including EPIC, lack sensitivity to infer both the imaginary refractive indices of inclusions and
703 their volume fractions, we must assume the imaginary refractive indices of inclusions to infer their
704 volume fractions. Here, we investigate the effect of this assumption on the inferred volume
705 fractions and assess the resulting uncertainties.

706 A total of three different BC datasets were considered (Fig 13a12a). “BC1”, which we used,
707 and “BC2” were derived from multiple measurements combined with the assumption that light-
708 absorbing carbon has a single refractive index and that variation can be expressed by the
709 Bruggeman effective-medium theory (Bond and Bergstrom, 2006). “BC3”, utilized in aerosol
710 modeling for AirMSPI analysis (Kalashnikova et al., 2018), was originally referred to as the “soot”
711 component of the Optical Properties of Aerosols and Clouds (OPAC) dataset described in Hess et
712 al. (1998). The value of k is between 0.4 and 0.8 and is spectrally invariant or nearly invariant.

713 We tested nine different BrC datasets (Fig 13b12b). “BrC1”, which we used, was derived
714 from organic carbon extracted from wood burning and SAFARI biomass smoke samples as
715 described in Kirchstetter et al. (2004). “BrC2” is an Air-MSPI retrieved value during the FIREX-
716 AQ campaign (O. Kalashnikova, personal communication, May 19, 2020). “BrC3” represents
717 aerosols emitted from the smoldering combustion of Boreal and Indonesian peatlands (Sumlin et
718 al., 2018). “BrC4”, “BrC5”, and “BrC6” represent water-insoluble BrC with relative humidity of
719 0%, 75%, and 99%, respectively, calculated by combining the upper curve of Sun et al. (2007) and
720 hygroscopic properties in Rissler et al. (2006). “BrC7”, “BrC8”, and “BrC9” are the same but
721 represent water-soluble BrC. These datasets were obtained from the Table of Aerosol Optics (TAO)
722 dataset within the framework of the Models, In situ, and Remote sensing of Aerosols (MIRA)
723 working group projects (<https://science.larc.nasa.gov/mira-wg/>).

724 Here, two smoke cases were analyzed: “Case 1” (k_0 of 0.007 and SAE of 2) and “Case 2”
725 (k_0 of 0.012 and SAE of 1.5), representing the most populated EPIC retrievals in the AERONET
726 validation over North America and Central Africa, respectively. For Case 1, the f_{BC} and f_{BrC} based
727 on our current assumptions are 0.011 and 0.112, respectively (marked with a “star” marker in dark
728 blue in Fig 13e12c). With different assumptions for inclusion properties, they have a range of
729 0.008-0.031 and 0.096-0.982, respectively. Less absorbing BC assumptions (i.e., smaller k) result
730 in increased f_{BC} to 0.012 (“BC2” and “BrC1”) and 0.018 (“BC3” and “BrC2”). The maximum

731 difference of f_{BC} is 0.013, with the lowest absorption in BrC (“BrC9”). The potential f_{BrC} values
732 exhibit greater variability. The f_{BrC} value with the current assumption (0.112) is one of the lowest
733 values among tested combinations and similar to those from “BrC2” and “BrC3”, which have
734 stronger absorption than others. The BrC assumptions with less absorbing properties show higher
735 f_{BrC} from 0.264 to 0.981. We also tested the spectral k for dark BrC obtained from the FIREX-AQ
736 campaign in the western US (Chakrabarty et al., 2023). They showed an estimated f_{BC} close to
737 zero because of the relatively high k of 0.1 at 680 nm. Case 2 is converted to higher f_{BC} (0.019)
738 and similar f_{BrC} (0.117) compared to Case 1 with the default assumption. The range of f_{BC} and
739 f_{BrC} from the different combinations is 0.016-0.047 and 0.101-0.980, respectively. It is essential
740 to acknowledge that inferring volume fractions and mass concentrations is based on assumed
741 inclusion properties, introducing some uncertainties. The assumed properties of BC and BrC will
742 need to be refined in future studies (e.g., a suggested concept in Kahn et al., 2017) to enhance the
743 accuracy of our findings.
744



745
 746 Fig 4312. Spectral imaginary refractive indices of (a) BC and (b) BrC.
 747 volume fractions for (c) “Case 1” (k_0 of 0.007 and SAE of 2) and (d) “Case 2” (k_0 of 0.012 and
 748 SAE of 1.5). The star, circle, and triangle symbols in (c) and (d) refer to different BC assumptions
 749 of “BC1”, “BC2”, and “BC3” in (a). The different colors in (c) and (d) refer to different BrC
 750 assumptions from “BrC1” to “BrC9” in (b).

751

752 5. Summary and conclusions

753 This study introduced a technique inferring the BC and BrC light-absorbing components
 754 of smoke aerosol by leveraging the spectral absorption retrieved in the MAIAC EPIC algorithm.

755 Spectral absorption retrievals allowed us to quantify the BC and BrC fractions, which were then
756 converted to column-integrated mass concentrations assuming the particle mass extinction
757 efficiency. We assumed that BC and BrC are internally mixed with a non-absorbing host
758 representing non-absorbing OC, sulfate, nitrate, or ammonium components, using the Maxwell
759 Garnett effective medium approximation.

760 We analyzed regional characteristics over North America and Central Africa in 2018,
761 utilizing all available MAIAC EPIC smoke property retrievals (AOD, spectral SSA, ALH, and BC
762 and BrC volume fractions and mass concentrations). Selected cases showed that smoke aerosols
763 emitted from wildfires over western North America exhibited extremely high AOD up to ~6 with
764 elevated ALH (6-7 km). Dynamic changes in spectral absorption and significant BrC components
765 were observed during continental-scale transport. The ~~EPIC~~-MAIAC EPIC products successfully
766 monitored the transport and evolution of smoke optical properties with high temporal resolution
767 during regional-to-continental-scale transport. Biomass-burning smoke over Central Africa
768 displayed higher absorption with greater BC and BrC fractions than North America, showing
769 seasonal changes in major source locations. They also showed less strong zonal transport with
770 ALH closer to the surface, and diurnal change in smoke amounts related to fire activities.

771 EPIC-retrieved AOD₄₄₃, SSA₄₄₃, SSA₆₈₀, and ALH agreed with collocated AERONET and
772 CALIOP measurements with *rmse* of 0.2, 0.03-0.04, 0.02-0.04, and 0.8-1.3 km, respectively, and
773 the overall accuracies were comparable to other operational satellite products such as OMI,
774 TROPOMI, and POLDER. Spatiotemporally integration of measurements revealed geographical
775 characteristics and distinct differences in optical properties, ALH, and inferred BC and BrC,
776 closely linked to burning types and meteorological conditions. Smoke from forest fires in western
777 North America shows SSA₄₄₃ of 0.92 with low BC volume fraction of 0.011 and high ALH with
778 larger standard deviation (2.2 ± 1.2 km). The wildfires and agricultural fires over the Mexico
779 region generated smoke with more absorption and lower ALH. The Savanna region in Central
780 Africa during August to October shows smoke properties with most absorbing with high BC and
781 BrC volume fractions (0.015 and 0.178, respectively) and lower ALH with smaller variation.
782 Smoke from tropical forests in Central Africa exhibits absorption between that of western US and
783 savanna regions and high ALH variability. The impact of assumed imaginary refractive indices of
784 BC and BrC in estimating their volume fractions was analyzed based on a literature survey,
785 presenting the corresponding uncertainty ranges of our retrievals.

786 Although we focused on North America and Central Africa, smoke aerosols have a
787 significant impact on air quality and climate globally. Future studies will extend the analysis to
788 other regions using almost a decade of EPIC measurements since 2015, with extensive validation
789 and error analysis using multiple measurements, including AERONET, CALIOP, and in-situ
790 aerosol composition data.

791 The MAIAC EPIC smoke aerosol components presented here could serve as valuable *a*
792 *priori* information for recent and upcoming satellite missions such as the Plankton, Aerosol, Cloud,
793 ocean Ecosystem (PACE; <https://pace.gsfc.nasa.gov/>) (Remer et al., 2019a, b), the Multi-Angle
794 Imager for Aerosols (MAIA; <https://maia.jpl.nasa.gov/>) (Diner et al., 2018), EPS-SG Multi-

795 Viewing Multi-Channel Multi-Polarisation Imaging (3MI) (Fougnie et al., 2018) and Atmosphere
796 Observing System (AOS; <https://aos.gsfc.nasa.gov/>), focusing on retrieving aerosol microphysical
797 and optical properties, and inferring chemical composition, with higher accuracy from multi-angle
798 polarization measurements. Integration of our results with other in-situ and remote sensing
799 measurements and models (e.g., Kahn et al., 2023) should enhance our understanding of smoke
800 aerosol aging processes, improve air quality monitoring and forecasting, and refine the
801 quantification of radiative forcing due to smoke aerosols on a global scale.

802 **Author contributions**

803 M. Choi and AL designed the study with discussions with GLS and SG. GLS provided
804 major guidance on developing the BC and BrC estimation algorithms. AL and WY provided the
805 MAIAC EPIC products. AL and SK conducted RT calculations (LUTs for MAIAC). M. Choi, AL,
806 YW and SG developed the code and performed the retrievals. GLS and OK participated in the
807 collection of refractive indices data. M. Choi, AL, GLS, and SG analyzed the results. M. Choi and
808 AL wrote the manuscript with comments from all co-authors.

809 **Competing interests**

810 The authors declare that they have no conflict of interest.

811 **Data availability**

812 The retrievals can be requested directly from the corresponding author
813 (myungje.choi@nasa.gov) or [Dr. Alexei Lyapustin \(alexey.i.lyapustin@nasa.gov\)](mailto:alexey.i.lyapustin@nasa.gov).

814 **Acknowledgment**

815 The work of A. Lyapustin, M. Choi, S. Go, and Y. Wang was funded by the NASA
816 DSCOVR program (21-DSCOVR-21-0004; manager Dr. R. Eckman) and in part by the NASA
817 PACE program (19-PACESAT19-0039). J. S Reid was funded by the Office of Naval Research,
818 Code 322. The work of H. Moosmüller was supported in part by the National Science Foundation
819 under Grant No. OIA- 2148788 and by NASA under grant 80NSSC20M0205 (PACE SAT Project:
820 PACE UV ROAD). We are grateful to the AERONET team for providing validation data and to
821 the NASA Center for Climate Simulations providing resources for the EPIC data processing.

822 **References**

823 Ahn, C., Torres, O., Jethva, H., Tiruchirapalli, R., and Huang, L.-K.: Evaluation of Aerosol
824 Properties Observed by DSCOVR/EPIC Instrument From the Earth-Sun Lagrange 1 Orbit, J.
825 Geophys. Res. Atmos., 126, e2020JD033651,

826 <https://doi.org/https://doi.org/10.1029/2020JD033651>, 2021.

827 Andreae, M. O.: Emission of trace gases and aerosols from biomass burning – an updated
828 assessment, *Atmos. Chem. Phys.*, 19, 8523–8546, <https://doi.org/10.5194/acp-19-8523-2019>,
829 2019.

830 Andreae, M. O. and Gelencsér, A.: Black carbon or brown carbon? the nature of light-absorbing
831 carbonaceous aerosols, *Atmos. Chem. Phys.*, 6, 3131–3148, <https://doi.org/10.5194/acp-6-3131-2006>, 2006.

832
833 Andreae, M. O. and Merlet, P.: Emission of trace gases and aerosols from biomass burning, *Global
834 Biogeochem. Cycles*, 15, 955–966, <https://doi.org/10.1029/2000GB001382>, 2001.

835 Bellouin, N., Boucher, O., Haywood, J., and Reddy, M. S.: Global estimate of aerosol direct
836 radiative forcing from satellite measurements, *Nature*, 438, 1138–1141,
837 <https://doi.org/10.1038/nature04348>, 2005.

838 Bhandari, J., China, S., Chandrakar, K. K., Kinney, G., Cantrell, W., Shaw, R. A., Mazzoleni, L.
839 R., Giroto, G., Sharma, N., Gorkowski, K., Gilardoni, S., Decesari, S., Facchini, M. C., Zanca,
840 N., Pavese, G., Esposito, F., Dubey, M. K., Aiken, A. C., Chakrabarty, R. K., Moosmüller,
841 H., Onasch, T. B., Zaveri, R. A., Scarnato, B. V., Fialho, P., and Mazzoleni, C.: Extensive
842 Soot Compaction by Cloud Processing from Laboratory and Field Observations, *Sci. Rep.*, 9,
843 <https://doi.org/10.1038/s41598-019-48143-y>, 2019.

844 Bohren, C. F. and Huffman, D. R.: *Absorption and Scattering of Light by Small Particles*, Wiley,
845 <https://doi.org/10.1002/9783527618156>, 1998.

846 Bond, T. C. and Bergstrom, R. W.: *Light Absorption by Carbonaceous Particles: An Investigative
847 Review*, *Aerosol Sci. Technol.*, 40, 27–67, <https://doi.org/10.1080/02786820500421521>,
848 2006.

849 Bond, T. C., Doherty, S. J., Fahey, D. W., Forster, P. M., Berntsen, T., Deangelo, B. J., Flanner,
850 M. G., Ghan, S., Kärcher, B., Koch, D., Kinne, S., Kondo, Y., Quinn, P. K., Sarofim, M. C.,
851 Schultz, M. G., Schulz, M., Venkataraman, C., Zhang, H., Zhang, S., Bellouin, N., Guttikunda,
852 S. K., Hopke, P. K., Jacobson, M. Z., Kaiser, J. W., Klimont, Z., Lohmann, U., Schwarz, J.
853 P., Shindell, D., Storelvmo, T., Warren, S. G., and Zender, C. S.: Bounding the role of black
854 carbon in the climate system: A scientific assessment, *J. Geophys. Res. Atmos.*, 118, 5380–
855 5552, <https://doi.org/10.1002/jgrd.50171>, 2013.

856 Bond, W. J. and Keeley, J. E.: Fire as a global “herbivore”: the ecology and evolution of flammable
857 ecosystems., *Trends Ecol. Evol.*, 20, 387–94, <https://doi.org/10.1016/j.tree.2005.04.025>,
858 2005.

859 Carter, T. S., Heald, C. L., Cappa, C. D., Kroll, J. H., Campos, T. L., Coe, H., Cotterell, M. I.,
860 Davies, N. W., Farmer, D. K., Fox, C., Garofalo, L. A., Hu, L., Langridge, J. M., Levin, E. J.
861 T., Murphy, S. M., Pokhrel, R. P., Shen, Y., Szpek, K., Taylor, J. W., and Wu, H.:
862 Investigating Carbonaceous Aerosol and Its Absorption Properties From Fires in the Western
863 United States (WE-CAN) and Southern Africa (ORACLES and CLARIFY), *J. Geophys. Res.
864 Atmos.*, 126, 647–650, <https://doi.org/10.1029/2021JD034984>, 2021.

865 Chakrabarty, R. K., Moosmüller, H., Chen, L.-W. A., Lewis, K., Arnott, W. P., Mazzoleni, C.,
866 Dubey, M. K., Wold, C. E., Hao, W. M., and Kreidenweis, S. M.: Brown carbon in tar balls
867 from smoldering biomass combustion, *Atmos. Chem. Phys.*, 10, 6363–6370,
868 <https://doi.org/10.5194/acp-10-6363-2010>, 2010.

869 Chakrabarty, R. K., Shetty, N. J., Thind, A. S., Beeler, P., Sumlin, B. J., Zhang, C., Liu, P., Idrobo,
870 J. C., Adachi, K., Wagner, N. L., Schwarz, J. P., Ahern, A., Sedlacek, A. J., Lambe, A., Daube,
871 C., Lyu, M., Liu, C., Herndon, S., Onasch, T. B., and Mishra, R.: Shortwave absorption by

872 wildfire smoke dominated by dark brown carbon, *Nat. Geosci.*,
873 <https://doi.org/10.1038/s41561-023-01237-9>, 2023.

874 Chen, C., Dubovik, O., Fuertes, D., Litvinov, P., Lapyonok, T., Lopatin, A., Ducos, F., Derimian,
875 Y., Herman, M., Tanré, D., Remer, L. A., Lyapustin, A., Sayer, A. M., Levy, R. C., Christina
876 Hsu, N., Descloitres, J., Li, L., Torres, B., Karol, Y., Herrera, M., Herreras, M., Aspetsberger,
877 M., Wanzenboeck, M., Bindreiter, L., Marth, D., Hangler, A., and Federspiel, C.: Validation
878 of GRASP algorithm product from POLDER/PARASOL data and assessment of multi-
879 angular polarimetry potential for aerosol monitoring, *Earth Syst. Sci. Data*, 12, 3573–3620,
880 <https://doi.org/10.5194/essd-12-3573-2020>, 2020.

881 Cheng, B., Alapaty, K., and Arunachalam, S.: Spatiotemporal trends in PM_{2.5} chemical
882 composition in the conterminous U.S. during 2006–2020, *Atmos. Environ.*, 316, 120188,
883 <https://doi.org/10.1016/j.atmosenv.2023.120188>, 2024.

884 Choi, Y., Ghim, Y. S., Zhang, Y., Park, S. M., and Song, I. H.: Estimation of surface concentrations
885 of black carbon from long-term measurements at aeronet sites over Korea, *Remote Sens.*, 12,
886 1–24, <https://doi.org/10.3390/rs12233904>, 2020.

887 Corbin, J. C., Modini, R. L., and Gysel-Beer, M.: Mechanisms of soot-aggregate restructuring and
888 compaction, *Aerosol Sci. Technol.*, 57, 89–111,
889 <https://doi.org/10.1080/02786826.2022.2137385>, 2023.

890 Dennison, P. E., Brewer, S. C., Arnold, J. D., and Moritz, M. A.: Large wildfire trends in the
891 western United States, 1984–2011, *Geophys. Res. Lett.*, 41, 2928–2933,
892 <https://doi.org/10.1002/2014GL059576>, 2014.

893 Diner, D. J., Boland, S. W., Brauer, M., Bruegge, C., Burke, K. A., Chipman, R., Di Girolamo, L.,
894 Garay, M. J., Hasheminassab, S., and Hyer, E.: Advances in multiangle satellite remote
895 sensing of speciated airborne particulate matter and association with adverse health effects:
896 from MISR to MAIA, *J. Appl. Remote Sens.*, 12, 1, <https://doi.org/10.1117/1.JRS.12.042603>,
897 2018.

898 Dubovik, O. and King, M. D.: A flexible inversion algorithm for retrieval of aerosol optical
899 properties from Sun and sky radiance measurements, *J. Geophys. Res. Atmos.*, 105, 20673–
900 20696, <https://doi.org/10.1029/2000JD900282>, 2000.

901 Dubovik, O., Holben, B., Eck, T. F., Smirnov, A., Kaufman, Y. J., King, M. D., Tanré, D., and
902 Slutsker, I.: Variability of Absorption and Optical Properties of Key Aerosol Types Observed
903 in Worldwide Locations, *J. Atmos. Sci.*, 59, 590–608, [https://doi.org/10.1175/1520-0469\(2002\)059<0590:VOAAOP>2.0.CO;2](https://doi.org/10.1175/1520-0469(2002)059<0590:VOAAOP>2.0.CO;2), 2002.

905 Dubovik, O., Sinyuk, A., Lapyonok, T., Holben, B. N., Mishchenko, M., Yang, P., Eck, T. F.,
906 Volten, H., Muñoz, O., Veihelmann, B., van der Zande, W. J., Leon, J. F., Sorokin, M., and
907 Slutsker, I.: Application of spheroid models to account for aerosol particle nonsphericity in
908 remote sensing of desert dust, *J. Geophys. Res. Atmos.*, 111, 1–34,
909 <https://doi.org/10.1029/2005JD006619>, 2006.

910 Dubovik, O., Herman, M., Holdak, A., Lapyonok, T., Tanré, D., Deuzé, J. L., Ducos, F., Sinyuk,
911 A., and Lopatin, A.: Statistically optimized inversion algorithm for enhanced retrieval of
912 aerosol properties from spectral multi-angle polarimetric satellite observations, *Atmos. Meas.
913 Tech.*, 4, 975–1018, <https://doi.org/10.5194/amt-4-975-2011>, 2011.

914 Dubovik, O., Lapyonok, T., Litvinov, P., Herman, M., Fuertes, D., Ducos, F., Torres, B., Derimian,
915 Y., Huang, X., Lopatin, A., Chaikovskiy, A., Aspetsberger, M., and Federspiel, C.: GRASP:
916 a versatile algorithm for characterizing the atmosphere, *SPIE Newsroom*,
917 <https://doi.org/10.1117/2.1201408.005558>, 2014.

- 918 Duncan, B. N., Martin, R. V., Staudt, A. C., Yevich, R., and Logan, J. A.: Interannual and seasonal
919 variability of biomass burning emissions constrained by satellite observations, *J. Geophys.*
920 *Res. Atmos.*, 108, <https://doi.org/10.1029/2002JD002378>, 2003.
- 921 Eck, T. F., Holben, B. N., Reid, J. S., Dubovik, O., Smirnov, A., O'Neill, N. T., Slutsker, I., and
922 Kinne, S.: Wavelength dependence of the optical depth of biomass burning, urban, and desert
923 dust aerosols, *J. Geophys. Res.*, 104, 31333, <https://doi.org/10.1029/1999JD900923>, 1999.
- 924 Eck, T. F., Holben, B. N., Ward, D. E., Mukelabai, M. M., Dubovik, O., Smirnov, A., Schafer, J.
925 S., Hsu, N. C., Piketh, S. J., Queface, A., Le Roux, J., Swap, R. J., and Slutsker, I.: Variability
926 of biomass burning aerosol optical characteristics in southern Africa during the SAFARI 2000
927 dry season campaign and a comparison of single scattering albedo estimates from radiometric
928 measurements, *J. Geophys. Res. Atmos.*, 108, <https://doi.org/10.1029/2002jd002321>, 2003.
- 929 Eck, T. F., Holben, B. N., Reid, J. S., Mukelabai, M. M., Piketh, S. J., Torres, O., Jethva, H. T.,
930 Hyer, E. J., Ward, D. E., Dubovik, O., Sinyuk, A., Schafer, J. S., Giles, D. M., Sorokin, M.,
931 Smirnov, A., and Slutsker, I.: A seasonal trend of single scattering albedo in southern African
932 biomass-burning particles: Implications for satellite products and estimates of emissions for
933 the world's largest biomass-burning source, *J. Geophys. Res. Atmos.*, 118, 6414–6432,
934 <https://doi.org/10.1002/jgrd.50500>, 2013.
- 935 Eck, T. F., Holben, B. N., Reid, J. S., Sinyuk, A., Giles, D. M., Arola, A., Slutsker, I., Schafer, J.
936 S., Sorokin, M. G., Smirnov, A., LaRosa, A. D., Kraft, J., Reid, E. A., O'Neill, N. T., Welton,
937 E. J., and Menendez, A. R.: The extreme forest fires in California/Oregon in 2020: Aerosol
938 optical and physical properties and comparisons of aged versus fresh smoke, *Atmos. Environ.*,
939 305, <https://doi.org/10.1016/j.atmosenv.2023.119798>, 2023.
- 940 Fougnie, B., Marbach, T., Lacan, A., Lang, R., Schlüssel, P., Poli, G., Munro, R., and Couto, A.
941 B.: The multi-viewing multi-channel multi-polarisation imager – Overview of the 3MI
942 polarimetric mission for aerosol and cloud characterization, *J. Quant. Spectrosc. Radiat.*
943 *Transf.*, 219, 23–32, <https://doi.org/10.1016/j.jqsrt.2018.07.008>, 2018.
- 944 Garnett, J. C. M.: XII. Colours in metal glasses and in metallic films, *Philos. Trans. R. Soc. London.*
945 *Ser. A, Contain. Pap. a Math. or Phys. Character*, 203, 385–420,
946 <https://doi.org/10.1098/rsta.1904.0024>, 1904.
- 947 Giles, D. M., Holben, B. N., Eck, T. F., Sinyuk, A., Smirnov, A., Slutsker, I., Dickerson, R. R.,
948 Thompson, A. M., and Schafer, J. S.: An analysis of AERONET aerosol absorption properties
949 and classifications representative of aerosol source regions, *J. Geophys. Res. Atmos.*, 117, 1–
950 16, <https://doi.org/10.1029/2012JD018127>, 2012.
- 951 Giles, D. M., Sinyuk, A., Sorokin, M. G., Schafer, J. S., Smirnov, A., Slutsker, I., Eck, T. F.,
952 Holben, B. N., Lewis, J. R., Campbell, J. R., Welton, E. J., Korokin, S. V., and Lyapustin, A.
953 I.: Advancements in the Aerosol Robotic Network (AERONET) Version 3 database –
954 automated near-real-time quality control algorithm with improved cloud screening for Sun
955 photometer aerosol optical depth (AOD) measurements, *Atmos. Meas. Tech.*, 12, 169–209,
956 <https://doi.org/10.5194/amt-12-169-2019>, 2019.
- 957 Go, S., Kim, J., Park, S. S., Kim, M., Lim, H., Kim, J. Y., Lee, D. W., and Im, J.: Synergistic use
958 of hyperspectral uv-visible omi and broadband meteorological imager modis data for a
959 merged aerosol product, *Remote Sens.*, 12, 1–34, <https://doi.org/10.3390/rs12233987>, 2020.
- 960 Go, S., Lyapustin, A., Schuster, G. L., Choi, M., Ginoux, P., Chin, M., Kalashnikova, O., Dubovik,
961 O., Kim, J., da Silva, A., Holben, B., and Reid, J. S.: Inferring iron-oxide species content in
962 atmospheric mineral dust from DSCOVER EPIC observations, *Atmos. Chem. Phys.*, 22, 1395–
963 1423, <https://doi.org/10.5194/acp-22-1395-2022>, 2022.

964 Gyawali, M., Arnott, W., Zaveri, R., Song, C., Flowers, B., Dubey, M., Setyan, A., Zhang, Q.,
965 China, S., Mazzoleni, C., Gorkowski, K., Subramanian, R., and Moosmüller, H.: Evolution
966 of Multispectral Aerosol Absorption Properties in a Biogenically-Influenced Urban
967 Environment during the CARES Campaign, *Atmosphere (Basel)*, 8, 217,
968 <https://doi.org/10.3390/atmos8110217>, 2017.

969 Haywood, J. M., Abel, S. J., Barrett, P. A., Bellouin, N., Blyth, A., Bower, K. N., Brooks, M.,
970 Carslaw, K., Che, H., Coe, H., Cotterell, M. I., Crawford, I., Cui, Z., Davies, N., Dingley, B.,
971 Field, P., Formenti, P., Gordon, H., de Graaf, M., Herbert, R., Johnson, B., Jones, A. C.,
972 Langridge, J. M., Malavelle, F., Partridge, D. G., Peers, F., Redemann, J., Stier, P., Szpek, K.,
973 Taylor, J. W., Watson-Parris, D., Wood, R., Wu, H., and Zuidema, P.: The CLOUD–Aerosol–
974 Radiation Interaction and Forcing: Year 2017 (CLARIFY-2017) measurement campaign,
975 *Atmos. Chem. Phys.*, 21, 1049–1084, <https://doi.org/10.5194/acp-21-1049-2021>, 2021.

976 Hess, M., Koepke, P., and Schult, I.: Optical Properties of Aerosols and Clouds: The Software
977 Package OPAC, *Bull. Am. Meteorol. Soc.*, 79, 831–844, [https://doi.org/10.1175/1520-0477\(1998\)079<0831:OPOAAC>2.0.CO;2](https://doi.org/10.1175/1520-0477(1998)079<0831:OPOAAC>2.0.CO;2), 1998.

979 Hobbs, P. V., Reid, J. S., Kotchenruther, R. A., Ferek, R. J., and Weiss, R.: Direct Radiative
980 Forcing by Smoke from Biomass Burning, *Science (80-.)*, 275, 1777–1778,
981 <https://doi.org/10.1126/science.275.5307.1777>, 1997.

982 Hoffer, A., Gelencsér, A., Guyon, P., Kiss, G., Schmid, O., Frank, G. P., Artaxo, P., and Andreae,
983 M. O.: Optical properties of humic-like substances (HULIS) in biomass-burning aerosols,
984 *Atmos. Chem. Phys.*, 6, 3563–3570, <https://doi.org/10.5194/acp-6-3563-2006>, 2006.

985 Holben, B. N., Eck, T. F., Slutsker, I., Tanré, D., Buis, J. P., Setzer, A., Vermote, E., Reagan, J.
986 A., Kaufman, Y. J., Nakajima, T., Lavenu, F., Jankowiak, I., and Smirnov, A.: AERONET—
987 A Federated Instrument Network and Data Archive for Aerosol Characterization, *Remote
988 Sens. Environ.*, 66, 1–16, [https://doi.org/10.1016/S0034-4257\(98\)00031-5](https://doi.org/10.1016/S0034-4257(98)00031-5), 1998.

989 IPCC: Climate Change 2021 – The Physical Science Basis, Cambridge University Press,
990 <https://doi.org/10.1017/9781009157896>, 2023.

991 Jacobson, M. Z.: Strong radiative heating due to the mixing state of black carbon in atmospheric
992 aerosols, *Nature*, 409, 695–697, <https://doi.org/10.1038/35055518>, 2001.

993 Jethva, H., Torres, O., and Ahn, C.: Global assessment of OMI aerosol single-scattering albedo
994 using ground-based AERONET inversion, *J. Geophys. Res.*, 119, 9020–9040,
995 <https://doi.org/10.1002/2014JD021672>, 2014.

996 Jo, D. S., Park, R. J., Lee, S., Kim, S. W., and Zhang, X.: A global simulation of brown carbon:
997 Implications for photochemistry and direct radiative effect, *Atmos. Chem. Phys.*, 16, 3413–
998 3432, <https://doi.org/10.5194/acp-16-3413-2016>, 2016.

999 Junghenn Noyes, K., Kahn, R., Sedlacek, A., Kleinman, L., Limbacher, J., and Li, Z.: Wildfire
1000 Smoke Particle Properties and Evolution, from Space-Based Multi-Angle Imaging, *Remote
1001 Sens.*, 12, 769, <https://doi.org/10.3390/rs12050769>, 2020a.

1002 Junghenn Noyes, K. T., Kahn, R. A., Limbacher, J. A., Li, Z., Fenn, M. A., Giles, D. M., Hair, J.
1003 W., Katich, J. M., Moore, R. H., Robinson, C. E., Sanchez, K. J., Shingler, T. J., Thornhill,
1004 K. L., Wiggins, E. B., and Winstead, E. L.: Wildfire Smoke Particle Properties and Evolution,
1005 From Space-Based Multi-Angle Imaging II: The Williams Flats Fire during the FIREX-AQ
1006 Campaign, *Remote Sens.*, 12, 3823, <https://doi.org/10.3390/rs12223823>, 2020b.

1007 Junghenn Noyes, K. T., Kahn, R. A., Limbacher, J. A., and Li, Z.: Canadian and Alaskan wildfire
1008 smoke particle properties, their evolution, and controlling factors, from satellite observations,
1009 *Atmos. Chem. Phys.*, 22, 10267–10290, <https://doi.org/10.5194/acp-22-10267-2022>, 2022.

1010 Kahn, R. A., Berkoff, T. A., Brock, C., Chen, G., Ferrare, R. A., Ghan, S., Hansico, T. F., Hegg,
1011 D. A., Martins, J. V., McNaughton, C. S., Murphy, D. M., Ogren, J. A., Penner, J. E.,
1012 Pilewskie, P., Seinfeld, J. H., and Worsnop, D. R.: SAM-CAAM: A Concept for Acquiring
1013 Systematic Aircraft Measurements to Characterize Aerosol Air Masses, *Bull. Am. Meteorol.*
1014 *Soc.*, 98, 2215–2228, <https://doi.org/10.1175/BAMS-D-16-0003.1>, 2017.

1015 Kahn, R. A., Andrews, E., Brock, C. A., Chin, M., Feingold, G., Gettelman, A., Levy, R. C.,
1016 Murphy, D. M., Nenes, A., Pierce, J. R., Popp, T., Redemann, J., Sayer, A. M., da Silva, A.
1017 M., Sogacheva, L., and Stier, P.: Reducing Aerosol Forcing Uncertainty by Combining
1018 Models With Satellite and Within-The-Atmosphere Observations: A Three-Way Street, *Rev.*
1019 *Geophys.*, 61, <https://doi.org/10.1029/2022RG000796>, 2023.

1020 Kalashnikova, O. V., Garay, M. J., Bates, K. H., Kenseth, C. M., Kong, W., Cappa, C. D.,
1021 Lyapustin, A. I., Jonsson, H. H., Seidel, F. C., Xu, F., Diner, D. J., and Seinfeld, J. H.:
1022 Photopolarimetric Sensitivity to Black Carbon Content of Wildfire Smoke: Results From the
1023 2016 ImPACT-PM Field Campaign, *J. Geophys. Res. Atmos.*, 123, 5376–5396,
1024 <https://doi.org/10.1029/2017JD028032>, 2018.

1025 Kirchstetter, T. W., Novakov, T., and Hobbs, P. V.: Evidence that the spectral dependence of light
1026 absorption by aerosols is affected by organic carbon, *J. Geophys. Res. D Atmos.*, 109, 1–12,
1027 <https://doi.org/10.1029/2004JD004999>, 2004.

1028 Kleinman, L. I., Sedlacek III, A. J., Adachi, K., Buseck, P. R., Collier, S., Dubey, M. K., Hodshire,
1029 A. L., Lewis, E., Onasch, T. B., Pierce, J. R., Shilling, J., Springston, S. R., Wang, J., Zhang,
1030 Q., Zhou, S., and Yokelson, R. J.: Rapid evolution of aerosol particles and their optical
1031 properties downwind of wildfires in the western US, *Atmos. Chem. Phys.*, 20, 13319–13341,
1032 <https://doi.org/10.5194/acp-20-13319-2020>, 2020.

1033 Lack, D. A., Langridge, J. M., Bahreini, R., Cappa, C. D., Middlebrook, A. M., and Schwarz, J.
1034 P.: Brown carbon and internal mixing in biomass burning particles, *Proc. Natl. Acad. Sci.*,
1035 109, 14802–14807, <https://doi.org/10.1073/pnas.1206575109>, 2012.

1036 Laskin, A., Laskin, J., and Nizkorodov, S. A.: Chemistry of Atmospheric Brown Carbon, *Chem.*
1037 *Rev.*, 115, 4335–4382, <https://doi.org/10.1021/cr5006167>, 2015.

1038 Lavoué, D., Liousse, C., Cachier, H., Stocks, B. J., and Goldammer, J. G.: Modeling of
1039 carbonaceous particles emitted by boreal and temperate wildfires at northern latitudes, *J.*
1040 *Geophys. Res. Atmos.*, 105, 26871–26890, <https://doi.org/10.1029/2000JD900180>, 2000.

1041 Lesins, G., Chylek, P., and Lohmann, U.: A study of internal and external mixing scenarios and
1042 its effect on aerosol optical properties and direct radiative forcing, *J. Geophys. Res. Atmos.*,
1043 107, <https://doi.org/10.1029/2001jd000973>, 2002.

1044 Levenberg, K.: A method for the solution of certain non-linear problems in least squares, *Q. Appl.*
1045 *Math.*, 2, 164–168, <https://doi.org/10.1090/qam/10666>, 1944.

1046 Li, L., Dubovik, O., Derimian, Y., Schuster, G. L., Lapyonok, T., Litvinov, P., Ducos, F., Fuertes,
1047 D., Chen, C., Li, Z., Lopatin, A., Torres, B., and Che, H.: Retrieval of aerosol components
1048 directly from satellite and ground-based measurements, *Atmos. Chem. Phys.*, 19, 13409–
1049 13443, <https://doi.org/10.5194/acp-19-13409-2019>, 2019.

1050 Li, L., Che, H., Derimian, Y., Dubovik, O., Schuster, G. L., Chen, C., Li, Q., Wang, Y., Guo, B.,
1051 and Zhang, X.: Retrievals of fine mode light-absorbing carbonaceous aerosols from
1052 POLDER/PARASOL observations over East and South Asia, *Remote Sens. Environ.*, 247,
1053 111913, <https://doi.org/10.1016/j.rse.2020.111913>, 2020.

1054 Li, L., Derimian, Y., Chen, C., Zhang, X., Che, H., Schuster, G. L., Fuertes, D., Litvinov, P.,
1055 Lapyonok, T., Lopatin, A., Matar, C., Ducos, F., Karol, Y., Torres, B., Gui, K., Zheng, Y.,

1056 Liang, Y., Lei, Y., Zhu, J., Zhang, L., Zhong, J., Zhang, X., and Dubovik, O.: Climatology of
1057 aerosol component concentrations derived from multi-angular polarimetric POLDER-3
1058 observations using GRASP algorithm, *Earth Syst. Sci. Data*, 14, 3439–3469,
1059 <https://doi.org/10.5194/essd-14-3439-2022>, 2022.

1060 Liang, Y., Stamatis, C., Fortner, E. C., Wernis, R. A., Van Rooy, P., Majluf, F., Yacovitch, T. I.,
1061 Daube, C., Herndon, S. C., Kreisberg, N. M., Barsanti, K. C., and Goldstein, A. H.: Emissions
1062 of organic compounds from western US wildfires and their near-fire transformations, *Atmos.*
1063 *Chem. Phys.*, 22, 9877–9893, <https://doi.org/10.5194/acp-22-9877-2022>, 2022.

1064 Lim, H.-J. and Turpin, B. J.: Origins of Primary and Secondary Organic Aerosol in Atlanta:
1065 Results of Time-Resolved Measurements during the Atlanta Supersite Experiment, *Environ.*
1066 *Sci. Technol.*, 36, 4489–4496, <https://doi.org/10.1021/es0206487>, 2002.

1067 Limbacher, J. A., Kahn, R. A., and Lee, J.: The new MISR research aerosol retrieval algorithm: a
1068 multi-angle, multi-spectral, bounded-variable least squares retrieval of aerosol particle
1069 properties over both land and water, *Atmos. Meas. Tech.*, 15, 6865–6887,
1070 <https://doi.org/10.5194/amt-15-6865-2022>, 2022.

1071 Liu, D., He, C., Schwarz, J. P., and Wang, X.: Lifecycle of light-absorbing carbonaceous aerosols
1072 in the atmosphere, *npj Clim. Atmos. Sci.*, 3, 40, [https://doi.org/10.1038/s41612-020-00145-](https://doi.org/10.1038/s41612-020-00145-8)
1073 [8](https://doi.org/10.1038/s41612-020-00145-8), 2020.

1074 Liu, Y., Stanturf, J., and Goodrick, S.: Trends in global wildfire potential in a changing climate,
1075 *For. Ecol. Manage.*, 259, 685–697, <https://doi.org/10.1016/j.foreco.2009.09.002>, 2010.

1076 Lyapustin, A., Wang, Y., Korkin, S., and Huang, D.: MODIS Collection 6 MAIAC algorithm,
1077 *Atmos. Meas. Tech.*, 11, 5741–5765, <https://doi.org/10.5194/amt-11-5741-2018>, 2018.

1078 Lyapustin, A., Wang, Y., Go, S., Choi, M., Korkin, S., Huang, D., Knyazikhin, Y., Blank, K., and
1079 Marshak, A.: Atmospheric Correction of DSCOVR EPIC: Version 2 MAIAC Algorithm,
1080 *Front. Remote Sens.*, 2, 1–10, <https://doi.org/10.3389/frsen.2021.748362>, 2021a.

1081 Lyapustin, A., Go, S., Korkin, S., Wang, Y., Torres, O., Jethva, H., and Marshak, A.: Retrievals
1082 of Aerosol Optical Depth and Spectral Absorption From DSCOVR EPIC, *Front. Remote*
1083 *Sens.*, 2, 1–14, <https://doi.org/10.3389/frsen.2021.645794>, 2021b.

1084 Markel, V. A.: Introduction to the Maxwell Garnett approximation: tutorial, *J. Opt. Soc. Am. A*,
1085 33, 1244, <https://doi.org/10.1364/josaa.33.001244>, 2016a.

1086 Markel, V. A.: Maxwell Garnett approximation (advanced topics): tutorial, *J. Opt. Soc. Am. A*, 33,
1087 2237, <https://doi.org/10.1364/josaa.33.002237>, 2016b.

1088 Marquardt, D. W.: An Algorithm for Least-Squares Estimation of Nonlinear Parameters, *J. Soc.*
1089 *Ind. Appl. Math.*, 11, 431–441, <https://doi.org/10.1137/0111030>, 1963.

1090 Marshak, A., Herman, J., Szabo, A., Blank, K., Carn, S., Cede, A., Geogdzhayev, I., Huang, D.,
1091 Huang, L. K., Knyazikhin, Y., Kowalewski, M., Krotkov, N., Lyapustin, A., McPeters, R.,
1092 Meyer, K. G., Torres, O., and Yang, Y.: Earth observations from DSCOVR epic instrument,
1093 *Bull. Am. Meteorol. Soc.*, 99, 1829–1850, <https://doi.org/10.1175/BAMS-D-17-0223.1>, 2018.

1094 Mok, J., Krotkov, N. A., Arola, A., Torres, O., Jethva, H., Andrade, M., Labow, G., Eck, T. F., Li,
1095 Z., Dickerson, R. R., Stenchikov, G. L., Osipov, S., and Ren, X.: Impacts of brown carbon
1096 from biomass burning on surface UV and ozone photochemistry in the Amazon Basin, *Sci.*
1097 *Rep.*, 6, 1–9, <https://doi.org/10.1038/srep36940>, 2016.

1098 Mok, J., Krotkov, N. A., Torres, O., Jethva, H., Li, Z., Kim, J., Koo, J. H., Go, S., Irie, H., Labow,
1099 G., Eck, T. F., Holben, B. N., Herman, J., Loughman, R. P., Spinei, E., Soo Lee, S., Khatri,
1100 P., and Campanelli, M.: Comparisons of spectral aerosol single scattering albedo in Seoul,
1101 South Korea, *Atmos. Meas. Tech.*, 11, 2295–2311, <https://doi.org/10.5194/amt-11-2295->

1102 2018, 2018.

1103 Moosmüller, H., Chakrabarty, R. K., and Arnott, W. P.: Aerosol light absorption and its
1104 measurement: A review, *J. Quant. Spectrosc. Radiat. Transf.*, 110, 844–878,
1105 <https://doi.org/10.1016/j.jqsrt.2009.02.035>, 2009.

1106 Nanda, S., de Graaf, M., Veeffkind, J. P., Sneep, M., ter Linden, M., Sun, J., and Levelt, P. F.: A
1107 first comparison of TROPOMI aerosol layer height (ALH) to CALIOP data, *Atmos. Meas.*
1108 *Tech.*, 13, 3043–3059, <https://doi.org/10.5194/amt-13-3043-2020>, 2020.

1109 Pausas, J. G. and Keeley, J. E.: A Burning Story: The Role of Fire in the History of Life, *Bioscience*,
1110 59, 593–601, <https://doi.org/10.1525/bio.2009.59.7.10>, 2009.

1111 Petters, M. D., Carrico, C. M., Kreidenweis, S. M., Prenni, A. J., DeMott, P. J., Collett, J. L., and
1112 Moosmüller, H.: Cloud condensation nucleation activity of biomass burning aerosol, *J.*
1113 *Geophys. Res. Atmos.*, 114, <https://doi.org/10.1029/2009JD012353>, 2009.

1114 Phillips, S. M. and Smith, G. D.: Light Absorption by Charge Transfer Complexes in Brown
1115 Carbon Aerosols, *Environ. Sci. Technol. Lett.*, 1, 382–386, <https://doi.org/10.1021/ez500263j>,
1116 2014.

1117 Pokhrel, R. P., Wagner, N. L., Langridge, J. M., Lack, D. A., Jayarathne, T., Stone, E. A.,
1118 Stockwell, C. E., Yokelson, R. J., and Murphy, S. M.: Parameterization of single-scattering
1119 albedo (SSA) and absorption Ångström exponent (AAE) with EC/OC for aerosol emissions
1120 from biomass burning, *Atmos. Chem. Phys.*, 16, 9549–9561, <https://doi.org/10.5194/acp-16-9549-2016>, 2016.

1122 Press, W. H., Teukolsky, S. A., Vetterling, W. T., and Flannery, B. P.: Numerical Recipes 3rd
1123 Edition: The Art of Scientific Computing, 3rd ed., Cambridge University Press, USA, 2007.

1124 Reid, J. S., Koppmann, R., Eck, T. F., and Eleuterio, D. P.: A review of biomass burning emissions
1125 part II: intensive physical properties of biomass burning particles, *Atmos. Chem. Phys.*, 5,
1126 799–825, <https://doi.org/10.5194/acp-5-799-2005>, 2005a.

1127 Reid, J. S., Eck, T. F., Christopher, S. A., Koppmann, R., Dubovik, O., Eleuterio, D. P., Holben,
1128 B. N., Reid, E. A., and Zhang, J.: A review of biomass burning emissions part III: intensive
1129 optical properties of biomass burning particles, *Atmos. Chem. Phys.*, 5, 827–849,
1130 <https://doi.org/10.5194/acp-5-827-2005>, 2005b.

1131 Remer, L. A., Davis, A. B., Mattoo, S., Levy, R. C., Kalashnikova, O. V., Coddington, O.,
1132 Chowdhary, J., Knobelspiesse, K., Xu, X., Ahmad, Z., Boss, E., Cairns, B., Dierssen, H. M.,
1133 Diner, D. J., Franz, B., Frouin, R., Gao, B., Ibrahim, A., Martins, J. V., Omar, A. H., Torres,
1134 O., Xu, F., and Zhai, P.-W.: Retrieving Aerosol Characteristics From the PACE Mission, Part
1135 1: Ocean Color Instrument, *Front. Earth Sci.*, 7, 1–20,
1136 <https://doi.org/10.3389/feart.2019.00152>, 2019a.

1137 Remer, L. A., Knobelspiesse, K., Zhai, P., Xu, F., Kalashnikova, O. V., Chowdhary, J., Hasekamp,
1138 O., Dubovik, O., Wu, L., Ahmad, Z., Boss, E., Cairns, B., Coddington, O., Davis, A. B.,
1139 Dierssen, H. M., Diner, D. J., Franz, B., Frouin, R., Gao, B., Ibrahim, A., Levy, R. C., Martins,
1140 J. V., Omar, A. H., and Torres, O.: Retrieving Aerosol Characteristics From the PACE
1141 Mission, Part 2: Multi-Angle and Polarimetry, *Front. Environ. Sci.*, 7, 1–21,
1142 <https://doi.org/10.3389/fenvs.2019.00094>, 2019b.

1143 Rios, B., Díaz-Esteban, Y., and Raga, G. B.: Smoke emissions from biomass burning in Central
1144 Mexico and their impact on air quality in Mexico City: May 2019 case study, *Sci. Total*
1145 *Environ.*, 904, 166912, <https://doi.org/10.1016/j.scitotenv.2023.166912>, 2023.

1146 Rissler, J., Vestin, A., Swietlicki, E., Fisch, G., Zhou, J., Artaxo, P., and Andreae, M. O.: Size
1147 distribution and hygroscopic properties of aerosol particles from dry-season biomass burning

1148 in Amazonia, *Atmos. Chem. Phys.*, 6, 471–491, <https://doi.org/10.5194/acp-6-471-2006>,
1149 2006.

1150 Samset, B. H., Stjern, C. W., Andrews, E., Kahn, R. A., Myhre, G., Schulz, M., and Schuster, G.
1151 L.: Aerosol Absorption: Progress Towards Global and Regional Constraints, *Curr. Clim.*
1152 *Chang. Reports*, 4, 65–83, <https://doi.org/10.1007/s40641-018-0091-4>, 2018.

1153 Sayer, A. M., Hsu, N. C., Eck, T. F., Smirnov, A., and Holben, B. N.: AERONET-based models
1154 of smoke-dominated aerosol near source regions and transported over oceans, and
1155 implications for satellite retrievals of aerosol optical depth, *Atmos. Chem. Phys.*, 14, 11493–
1156 11523, <https://doi.org/10.5194/acp-14-11493-2014>, 2014.

1157 Sayer, A. M., Hsu, N. C., Lee, J., Kim, W. V., Burton, S., Fenn, M. A., Ferrare, R. A.,
1158 Kacenelenbogen, M., LeBlanc, S., Pistone, K., Redemann, J., Segal-Rozenhaimer, M.,
1159 Shinozuka, Y., and Tsay, S.: Two decades observing smoke above clouds in the south-eastern
1160 Atlantic Ocean: Deep Blue algorithm updates and validation with ORACLES field campaign
1161 data, *Atmos. Meas. Tech.*, 12, 3595–3627, <https://doi.org/10.5194/amt-12-3595-2019>, 2019.

1162 Schroeder, W. and Giglio, L.: VIIRS/NPP Thermal Anomalies/Fire Daily L3 Global 1km SIN
1163 Grid V001. distributed by NASA EOSDIS Land Processes DAAC,
1164 [doi:10.5067/VIIRS/VNP14A1.001](https://doi.org/10.5067/VIIRS/VNP14A1.001), 2018.

1165 Schuster, G. L., Dubovik, O., Holben, B. N., and Clothiaux, E. E.: Inferring black carbon content
1166 and specific absorption from Aerosol Robotic Network (AERONET) aerosol retrievals, *J.*
1167 *Geophys. Res. D Atmos.*, 110, 1–19, <https://doi.org/10.1029/2004JD004548>, 2005.

1168 Schuster, G. L., Dubovik, O., and Arola, A.: Remote sensing of soot carbon – Part 1:
1169 Distinguishing different absorbing aerosol species, *Atmos. Chem. Phys.*, 16, 1565–1585,
1170 <https://doi.org/10.5194/acp-16-1565-2016>, 2016.

1171 Schwarz, J. P., Gao, R. S., Spackman, J. R., Watts, L. A., Thomson, D. S., Fahey, D. W., Ryerson,
1172 T. B., Peischl, J., Holloway, J. S., Trainer, M., Frost, G. J., Baynard, T., Lack, D. A., de Gouw,
1173 J. A., Warneke, C., and Del Negro, L. A.: Measurement of the mixing state, mass, and optical
1174 size of individual black carbon particles in urban and biomass burning emissions, *Geophys.*
1175 *Res. Lett.*, 35, <https://doi.org/10.1029/2008GL033968>, 2008.

1176 Seiler, W. and Crutzen, P. J.: Estimates of gross and net fluxes of carbon between the biosphere
1177 and the atmosphere from biomass burning, *Clim. Change*, 2, 207–247,
1178 <https://doi.org/10.1007/BF00137988>, 1980.

1179 Sengupta, D., Samburova, V., Bhattarai, C., Kirillova, E., Mazzoleni, L., Iaukea-Lum, M., Watts,
1180 A., Moosmüller, H., and Khlystov, A.: Light absorption by polar and non-polar aerosol
1181 compounds from laboratory biomass combustion, *Atmos. Chem. Phys.*, 18, 10849–10867,
1182 <https://doi.org/10.5194/acp-18-10849-2018>, 2018.

1183 Sengupta, D., Samburova, V., Bhattarai, C., Watts, A. C., Moosmüller, H., and Khlystov, A. Y.:
1184 Polar semivolatile organic compounds in biomass-burning emissions and their chemical
1185 transformations during aging in an oxidation flow reactor, *Atmos. Chem. Phys.*, 20, 8227–
1186 8250, <https://doi.org/10.5194/acp-20-8227-2020>, 2020.

1187 Sinyuk, A., Holben, B. N., Eck, T. F., Giles, D. M., Slutsker, I., Korkin, S., Schafer, J. S., Smirnov,
1188 A., Sorokin, M., and Lyapustin, A.: The AERONET Version 3 aerosol retrieval algorithm,
1189 associated uncertainties and comparisons to Version 2, *Atmos. Meas. Tech.*, 13, 3375–3411,
1190 <https://doi.org/10.5194/amt-13-3375-2020>, 2020.

1191 Sinyuk, A., Holben, B. N., Eck, T. F., Giles, D. M., Slutsker, I., Dubovik, O., Schafer, J. S.,
1192 Smirnov, A., and Sorokin, M.: Employing relaxed smoothness constraints on imaginary part
1193 of refractive index in AERONET aerosol retrieval algorithm, *Atmos. Meas. Tech.*, 15, 4135–

1194 4151, <https://doi.org/10.5194/amt-15-4135-2022>, 2022.

1195 Sumlin, B. J., Heinson, Y. W., Shetty, N., Pandey, A., Pattison, R. S., Baker, S., Hao, W. M., and
1196 Chakrabarty, R. K.: UV–Vis–IR spectral complex refractive indices and optical properties of
1197 brown carbon aerosol from biomass burning, *J. Quant. Spectrosc. Radiat. Transf.*, 206, 392–
1198 398, <https://doi.org/10.1016/j.jqsrt.2017.12.009>, 2018.

1199 Sun, H., Biedermann, L., and Bond, T. C.: Color of brown carbon: A model for ultraviolet and
1200 visible light absorption by organic carbon aerosol, *Geophys. Res. Lett.*, 34, L17813,
1201 <https://doi.org/10.1029/2007GL029797>, 2007.

1202 Swap, R. J., Annegarn, H. J., Suttles, J. T., King, M. D., Platnick, S., Privette, J. L., and Scholes,
1203 R. J.: Africa burning: A thematic analysis of the Southern African Regional Science Initiative
1204 (SAFARI 2000), *J. Geophys. Res. Atmos.*, 108, n/a-n/a,
1205 <https://doi.org/10.1029/2003JD003747>, 2003.

1206 Torres, O., Bhartia, P. K., Herman, J. R., Ahmad, Z., and Gleason, J.: Derivation of aerosol
1207 properties from satellite measurements of backscattered ultraviolet radiation: Theoretical
1208 basis, *J. Geophys. Res. Atmos.*, 103, 17099–17110, <https://doi.org/10.1029/98JD00900>, 1998.

1209 Torres, O., Tanskanen, A., Veihelmann, B., Ahn, C., Braak, R., Bhartia, P. K., Veeffkind, P., and
1210 Levelt, P.: Aerosols and surface UV products from Ozone Monitoring Instrument
1211 observations: An overview, *J. Geophys. Res. Atmos.*, 112, 1–14,
1212 <https://doi.org/10.1029/2007JD008809>, 2007.

1213 Torres, O., Ahn, C., and Chen, Z.: Improvements to the OMI near-UV aerosol algorithm using A-
1214 train CALIOP and AIRS observations, *Atmos. Meas. Tech.*, 6, 3257–3270,
1215 <https://doi.org/10.5194/amt-6-3257-2013>, 2013.

1216 Torres, O., Jethva, H., Ahn, C., Jaross, G., and Loyola, D. G.: TROPOMI aerosol products:
1217 Evaluation and observations of synoptic-scale carbonaceous aerosol plumes during 2018-
1218 2020, *Atmos. Meas. Tech.*, 13, 6789–6806, <https://doi.org/10.5194/amt-13-6789-2020>, 2020.

1219 Tritscher, T., Jurányi, Z., Martin, M., Chirico, R., Gysel, M., Heringa, M. F., DeCarlo, P. F., Sierau,
1220 B., Prévôt, A. S. H., Weingartner, E., and Baltensperger, U.: Changes of hygroscopicity and
1221 morphology during ageing of diesel soot, *Environ. Res. Lett.*, 6, 034026,
1222 <https://doi.org/10.1088/1748-9326/6/3/034026>, 2011.

1223 Turpin, B. J. and Lim, H.-J.: Species Contributions to PM_{2.5} Mass Concentrations: Revisiting
1224 Common Assumptions for Estimating Organic Mass, *Aerosol Sci. Technol.*, 35, 602–610,
1225 <https://doi.org/10.1080/02786820119445>, 2001.

1226 Wang, L., Li, Z., Tian, Q., Ma, Y., Zhang, F., Zhang, Y., Li, D., Li, K., and Li, L.: Estimate of
1227 aerosol absorbing components of black carbon, brown carbon, and dust from ground-based
1228 remote sensing data of sun-sky radiometers, *J. Geophys. Res. Atmos.*, 118, 6534–6543,
1229 <https://doi.org/10.1002/jgrd.50356>, 2013.

1230 Wang, X., Heald, C. L., Sedlacek, A. J., de Sá, S. S., Martin, S. T., Alexander, M. L., Watson, T.
1231 B., Aiken, A. C., Springston, S. R., and Artaxo, P.: Deriving brown carbon from
1232 multiwavelength absorption measurements: method and application to AERONET and
1233 Aethalometer observations, *Atmos. Chem. Phys.*, 16, 12733–12752,
1234 <https://doi.org/10.5194/acp-16-12733-2016>, 2016.

1235 Ward, D. E., Hao, W. M., Susott, R. A., Babbitt, R. E., Shea, R. W., Kauffman, J. B., and Justice,
1236 C. O.: Effect of fuel composition on combustion efficiency and emission factors for African
1237 savanna ecosystems, *J. Geophys. Res. Atmos.*, 101, 23569–23576,
1238 <https://doi.org/10.1029/95JD02595>, 1996.

1239 van der Werf, G. R., Randerson, J. T., Giglio, L., Collatz, G. J., Mu, M., Kasibhatla, P. S., Morton,

1240 D. C., DeFries, R. S., Jin, Y., and van Leeuwen, T. T.: Global fire emissions and the
1241 contribution of deforestation, savanna, forest, agricultural, and peat fires (1997–2009), *Atmos.*
1242 *Chem. Phys.*, 10, 11707–11735, <https://doi.org/10.5194/acp-10-11707-2010>, 2010.

1243 van der Werf, G. R., Randerson, J. T., Giglio, L., van Leeuwen, T. T., Chen, Y., Rogers, B. M.,
1244 Mu, M., van Marle, M. J. E., Morton, D. C., Collatz, G. J., Yokelson, R. J., and Kasibhatla,
1245 P. S.: Global fire emissions estimates during 1997–2016, *Earth Syst. Sci. Data*, 9, 697–720,
1246 <https://doi.org/10.5194/essd-9-697-2017>, 2017.

1247 Wooster, M. J., Roberts, G. J., Giglio, L., Roy, D., Freeborn, P., Boschetti, L., Justice, C., Ichoku,
1248 C., Schroeder, W., Davies, D., Smith, A., Setzer, A., Csiszar, I., Strydom, T., Frost, P., Zhang,
1249 T., Xu, W., de Jong, M., Johnston, J., Ellison, L., Vadrevu, K., McCarty, J., Tanpipat, V.,
1250 Schmidt, C., and San-Miguel, J.: Satellite remote sensing of active fires: History and current
1251 status, applications and future requirements, <https://doi.org/10.1016/j.rse.2021.112694>, 15
1252 December 2021.

1253 Xiong, R., Li, J., Zhang, Y., Zhang, L., Jiang, K., Zheng, H., Kong, S., Shen, H., Cheng, H., Shen,
1254 G., and Tao, S.: Global brown carbon emissions from combustion sources, *Environ. Sci.*
1255 *Ecotechnology*, 12, 100201, <https://doi.org/10.1016/j.ese.2022.100201>, 2022.

1256 Xu, X., Wang, J., Wang, Y., Zeng, J., Torres, O., Reid, J. S., Miller, S. D., Martins, J. V., and
1257 Remer, L. A.: Detecting layer height of smoke aerosols over vegetated land and water
1258 surfaces via oxygen absorption bands: hourly results from EPIC/DSCOVR in deep space,
1259 *Atmos. Meas. Tech.*, 12, 3269–3288, <https://doi.org/10.5194/amt-12-3269-2019>, 2019.

1260 Yu, H., Liu, S. C., and Dickinson, R. E.: Radiative effects of aerosols on the evolution of the
1261 atmospheric boundary layer, *J. Geophys. Res. Atmos.*, 107,
1262 <https://doi.org/10.1029/2001JD000754>, 2002.

1263 Zhang, A., Wang, Y., Zhang, Y., Weber, R. J., Song, Y., Ke, Z., and Zou, Y.: Modeling the global
1264 radiative effect of brown carbon: a potentially larger heating source in the tropical free
1265 troposphere than black carbon, *Atmos. Chem. Phys.*, 20, 1901–1920,
1266 <https://doi.org/10.5194/acp-20-1901-2020>, 2020.

1267